

Energy and momentum transfer of He atoms scattered from a lithium fluoride crystal surface

H. Legge

Deutsche Forschungsanstalt für Luft- und Raumfahrt, Bunsenstrasse 10, 37073 Göttingen, Germany

J. R. Manson

Department of Physics and Astronomy, Clemson University, Clemson, South Carolina 29634

J. P. Toennies

Max Planck Institut für Strömungsforschung, Bunsenstrasse 10, 37073 Göttingen, Germany

(Received 9 February 1998; accepted 7 January 1999)

Both the energy transfer and the normal and tangential force coefficients for scattering of a nearly monoenergetic beam of He atoms (incident energy $E_i=63$ meV) from a clean single crystal LiF(001) surface have been measured under wind tunnel conditions in the range of surface temperatures from 300 to 720 K. Expressions are derived for the differential reflection coefficient for a realistic He-LiF(001) potential with the inclusion of multiphonon processes, and these expressions are used to calculate the average energy and momentum transfers as well as their higher moments. The comparisons between theory and experiment indicate the presence of a moderate degree of surface roughness. The measured recovery temperature depends on incident beam angle and is significantly larger than expected for complete or partial accommodation, in good agreement with the theoretical calculations. © 1999 American Institute of Physics. [S0021-9606(99)70314-4]

I. INTRODUCTION

Under conditions of rarefied flow, the gas-surface interaction is usually described in terms of averaged properties such as the average energy exchange with the surface or the average momentum exchange in a particular direction.¹ These measurable quantities are often expressed in terms of dimensionless coefficients such as the energy exchange coefficient, the lift and drag coefficients, and accommodation coefficients for the momentum and energy.²⁻⁶ Despite considerable theoretical and experimental work over many decades, these accommodation coefficients are still poorly understood. For heavier atomic gases and technologically relevant surfaces, the energy accommodation coefficients are usually unity, a value which is consistent with contaminated and microscopically rough surfaces on which the incoming gas is brought to thermal equilibrium.^{3,7} For atomically clean surfaces few measurements have been reported.³ The available data suggest that under these conditions, and particularly with light gas atoms, the energy accommodation coefficients are significantly less than unity, and in some cases, such as for the scattering of He or H₂ at low temperatures, the values can be even as small as 0.1.^{3,8}

The recently developed high vacuum molecular beam wind tunnel apparatus used in the present experiments is a unique facility which makes it possible to study directly the momentum and energy transfer to a small sample impacted by an intense directed beam of atoms or molecules.⁹ The room temperature He atom beam used here had a speed ratio of approximately 14 and a very high Knudsen number of about $K_{n0}=4$ at the surface. The freshly cleaved (001) face of a single crystal of LiF served as a clean and well ordered surface.¹⁰ The order and cleanliness of the surface was sub-

sequently characterized in a separate ultrahigh vacuum (UHV) helium atom surface scattering apparatus by high resolution He atom diffraction. The large gas flow rate and the large area of the crystal face enabled measurements of total energy exchange and measurements of the normal and tangential force exerted by the gas beam on the crystal over a temperature range from 300 to 720 K. LiF was chosen as the target because, (1) it is the standard benchmark used in the field of atom-surface scattering,¹¹⁻¹⁷ (2) it has been demonstrated to be clean (and very importantly, free of adsorbed water) under the vacuum conditions of somewhat better than 10^{-5} Torr maintained in the wind tunnel chamber used in these experiments,^{14,15} and (3) the He-LiF (001) interaction potential has been extensively studied both experimentally¹⁷⁻²⁰ and theoretically.^{21,22} Preliminary results of these experiments were reported in Refs. 23 and 24.

These new experimental results on heat transfer coefficients and normal and tangential force coefficients are compared with a recently developed theory for the inelastic scattering of atomic projectiles by surfaces under conditions in which the total transferred energy can be large.^{25,26} Although the scattering conditions of this experiment indicate the exchange of many quanta of energy and hence are nearly classical, important quantum features such as diffraction are accounted for by the theory. The quantum mechanical treatment used also has the advantage that recoil effects which arise from the zero point motion are correctly accounted for.

Beginning from a completely quantum mechanical treatment of the elementary scattering process, a semiclassical and a classical limit for the microscopic differential reflection coefficient are calculated for the accurately known interaction potential of a He atom with the LiF(001) surface.^{17,18}

Three major dynamical approximations are involved: (1) taking linear coupling of the incident projectile with the vibrational displacement field of the crystal, (2) using only classically allowed paths for the projectile, and (3) making the "quick collision" approximation in which the collision time is assumed to be shorter than the period of a typical lattice vibration.^{24,25} The experimental data are compared with a semiclassical multilobe model in which an inelastic lobe of scattered particles is associated with each of the quantum mechanical diffraction peaks. This semiclassical limit goes over to the classical case in the correspondence principle limit of high energies and large temperatures where the diffraction peak intensities become negligible. With this model, the average properties of the scattered gas such as the average energy, average momenta, or higher moments of these quantities, are readily obtained from the differential reflection coefficient. All measured quantities, such as the accommodation or force coefficients, are simple functions of these averaged quantities. The theoretical model gives excellent agreement with the energy exchange coefficient at all measured incident angles and surface temperatures. The calculated values of the energy exchange coefficient imply energy accommodation coefficient values significantly less than unity.

Whereas the predicted normal force coefficients are somewhat larger than the measured values, the predicted tangential force coefficient is significantly too small. However, calculations for rough and highly corrugated surfaces agree with the measured normal and tangential force coefficients and this is taken as evidence that the measured force coefficients may be influenced to some extent by surface defects and surface roughness. The rough-surface calculations agree well with the experimental data both as a function of incident angle and as a function of temperature. The calculations for an ordered surface, while not predicting the magnitudes of the force coefficients correctly, do, however, give good results for the slopes of the temperature dependence.

The next section discusses the experiment in detail. The theory is developed in Sec. III and in Appendix A. Section IV contains a discussion of the experimental results and the comparison with the predictions of the theory. The concluding Sec. V summarizes the physical and technological information which can be obtained from such experiments and discusses possible future developments.

II. EXPERIMENT

The heat and force coefficient experiments were carried out in the molecular beam high vacuum wind tunnel V3G at the DLR in Göttingen.⁹ Figure 1 shows a schematic drawing of the sample holder and sample. The free jet He atom beam source was a thin-walled orifice 3.96 mm in diameter which was always operated at a stagnation temperature $T_0 = 300$ K with a typical stagnation pressure of $P_0 = 6.7$ mbar. The beam velocity was 1740 m/s, which corresponds to an incident beam energy of 63 meV (stagnation temperature $T_0 = 300$ K) and the speed ratio was 14.2. For all results presented here, the free stream density Knudsen number K_{n0} measured at the crystal face was equal to or greater than 4.3. This Knudsen number is given by

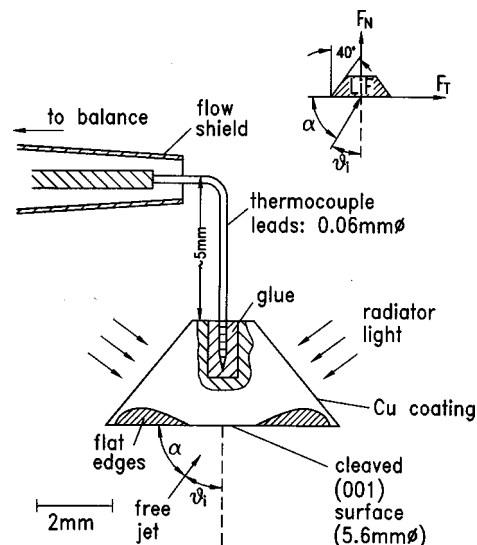


FIG. 1. Schematic diagram of the sample and sample holder showing the LiF conically shaped crystal sample disk and its mounting via a thermocouple to a microbalance. The inset shows the scattering angles and the directions of the normal and tangential force components F_n and F_t .

$$K_{n0} = 3.2 \frac{\mu_0}{\rho d \sqrt{2\pi R T_0}}, \quad (1)$$

where ρ is the free stream density, μ_0 is the viscosity at the stagnation temperature, d is the diameter of the crystal face, and R is the gas constant. The large wind tunnel chamber has a diameter of approximately 1.5 m with a length of 3 m. The crystal sample was placed about 4 cm from the orifice and the beam was not collimated, thus the entire crystal sample face was illuminated.

The conically shaped crystal samples had a square surface of 5×5 mm with rounded corners (see Fig. 2). The total mass of the crystals was typically 86 mg and the surface area of the experimental face of the crystal used in most of the experiments was 22.57 mm^2 . These conical samples were

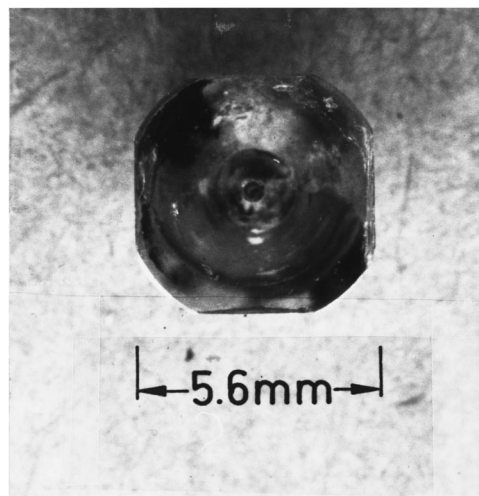


FIG. 2. Photograph of the cleaved (001) face of one of the LiF crystals as seen by the free jet. The actual linear dimension was about 5.6 mm, or approximately one-fourth of the size shown.

produced by cleavage through the central plane of a larger object with the shape of two identical cones attached at their bases. This object was produced by grinding a parallelepiped shaped LiF single crystal of high purity obtained from the Karl Korth company.²⁷ Only by cleaving such a C_{2v} symmetric object exactly through the middle is there a high probability of obtaining a clean cleave without broken edges.²⁸ The crystal was cleaved in the laboratory and subsequently mounted as fast as possible.

The morphology of cleaved alkali-halide crystal surfaces has been extensively studied also as a function of the surface temperature.²⁹⁻³⁴ Unfortunately, only a few studies provide quantitative information on the defect density at an atomic level. From high resolution scattering experiments on vacuum cleaved crystals, step densities of the order of $3 \times 10^{-3} \text{ \AA}^{-1}$ have been estimated.^{35,36}

The conical sides of the samples were coated from the top with Cu by vacuum deposition to assure good absorption of UV radiation. Two radiators located to the side and rear of the sample (see Fig. 1) were used to bake out the crystal and also to heat the crystal during the experiments.

After several test experiments, the following optimal pump-down procedure was used. First, the inner walls of the wind tunnel were completely cleaned with methanol. After mounting the sample holder and sample, the wind tunnel was evacuated slowly to avoid condensation of the remaining gas inside the vacuum chamber. The baffles and shields inside the vacuum chamber were cooled by liquid N_2 during evacuation in order to trap out oil and other contaminants back streaming from the diffusion pump. For the same reason, the crystal was heated to about 120 °C. Because of the intricate mounting procedures, typically three hours elapsed before the crystal was under vacuum. In order to remove impurities it was then baked for 1.5 hours at about 750 K and again after about 12-hour intervals.

The crystal was mounted on a specially designed two-component microbalance, by which the normal and tangential forces F_n and F_t were measured. The heat transfer was measured by a transient heat transfer technique using the entire LiF sample itself as a calorimeter.⁹ The atom beam source could be moved on a circle by a traversing mechanism around the disk center in order to vary the angle of incidence of the atom beam (see inset of Fig. 1). The distance between the jet orifice and the disk center was fixed at 40 mm. The whole apparatus was mounted in a frame which was protected by dampers from the vibrations of the large root pumps used to evacuate the tunnel. The test gas was helium of 99.9996 vol. % purity. The force and heat transfer measurements were made simultaneously. A complete account of the measurements and further technical details are given in Ref. 9.

Several factors lead to possible experimental errors in these measurements, which are larger than those expected from more traditional He atom scattering (HAS) experiments. Because of the need to work quickly in order to avoid contamination, there was not enough time for the usual time consuming careful alignment of the target. The target shape of a cone with the rear face considerably smaller in area than the experimentally measured face was chosen to avoid scat-

tering from the sides. However, the process of cleavage inadvertently left small faces at the edges of the front face which were tilted at angles (see Fig. 2) which could be struck by parts of the incoming atom beam at the largest angles of incidence. The overall accuracy of the heat transfer data is conservatively estimated to be $\pm 30\%$, while the accuracy of the force measurements is deemed to be $\pm 10\%$ near normal incidence and $\pm 15\%$ at the largest incidence angles of $\theta_i \approx 30^\circ$. There are possibly even larger errors in the tangential force constants due to parts of the beam striking the small cleavage planes on the sides of the sample. The uncertainty in the angle of incidence is estimated to be less than $\pm 5^\circ$.

As a control on the microscopic order and cleanliness of the samples, after the wind tunnel investigations the crystal was removed from the apparatus and immediately transferred in an evacuated glass excicator to the ultrahigh vacuum (UHV) HAS apparatus at the nearby Max Planck Institut laboratory. The HAS apparatus is similar to that described in detail in Refs. 37 and 38. After mounting, the sample was again baked in UHV to a temperature of 750 K in the HAS apparatus for 10 minutes to remove contamination arising during transport and pump down after mounting. Subsequently, total intensity angular distributions and time-of-flight (TOF) spectra were measured in the HAS apparatus at two beam energies of 63 and 37 meV. The angular distributions exhibited sharp specular and first-order diffraction peaks as well as small second-order diffraction peaks, and a small background similar to the best reported previously in the literature,³⁸⁻⁴¹ indicating good long-range order of the crystal face.

An example of one of the total intensity angular scans is shown in Fig. 3. The He beam is incident along the $\langle 110 \rangle$ azimuth, the surface temperature is $T_s = 298 \text{ K}$, and the energy is 68 meV. The points also shown in Fig. 3 are calculations for determining the surface corrugation and are discussed below in Sec. IVA. The insert shows a typical time-of-flight measurement, after transforming to energy transfer, and was taken at $E_i = 37 \text{ meV}$ and at an incident angle $\theta_i = 64^\circ$. This and all the other measured TOF spectra exhibited very sharp inelastic peaks due to creation and annihilation of Rayleigh mode phonons, and a rather small diffuse elastic peak which indicates the presence of a small concentration of adsorbates or other disorder defects on the surface, similar in relative intensity as in results published previously.³⁸⁻⁴¹

III. THEORY

A. Differential reflection coefficient

The fraction of particles incident with momentum \mathbf{p}_i which are scattered into the solid angle $d\Omega_f$ centered on the direction of the final momentum \mathbf{p}_f and into the energy interval dE_f lying between E_f and $E_f + dE_f$ ($E_f = \mathbf{p}_f^2/2m$ where m is its mass) is given by the differential reflection coefficient $dR(\mathbf{p}_f, \mathbf{p}_i)/dE_f d\Omega_f$. The differential reflection coefficient is customarily normalized with respect to the incident flux normal to the surface. As shown in Fig. 4, the z -axis is normal to the surface and the incident and final polar angles θ_i and θ_f are measured with respect to the sur-

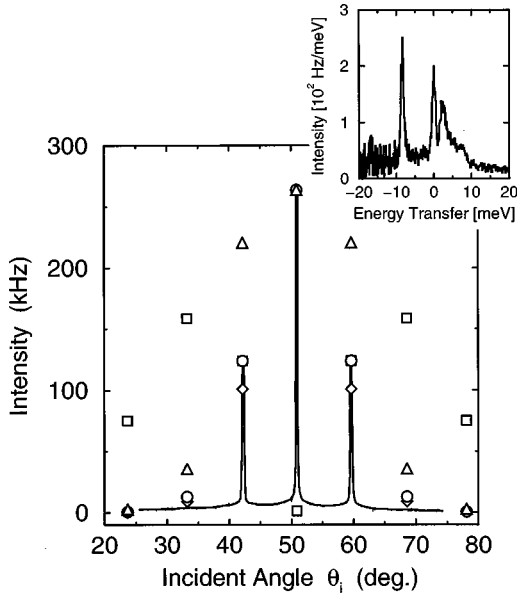


FIG. 3. An example of an angular distribution showing the diffraction peaks observed in the HAS apparatus. The solid line is the total measured scattered intensity as a function of incident angle for the (110) azimuth and an incident energy of 68 meV. The insert shows a time-of-flight spectrum, converted to energy transfer, taken in the (100) azimuth at an incident energy of 37 meV and at the incident angle $\theta_i = 64^\circ$. The surface temperature is 298 K in both cases. Several calculations based on the eikonal approximation, as discussed below in Sec. IVA are also shown. Relative diffraction intensity calculations for a corrugation parameter $A = 0.065$, (\diamond); for $A = 0.07$, (\circ); for $A = 0.085$, (\triangle); and for $A = 0.145$ Å, (\square) are shown for comparison. The $A = 0.07$ Å corrugation agrees a little better than the $A = 0.065$ Å for the first-order peak, but overestimates the very weak second-order peak.

face normal. Moreover, the total momentum \mathbf{p}_q (where $q = i$ or f) is composed of components p_{qz} perpendicular to the surface and \mathbf{P}_q parallel to the surface, i.e., $\mathbf{p}_q = (\mathbf{P}_q, p_{qz})$. Then the incident normal flux is proportional to p_{iz} .

Since the differential reflection coefficient specifies the angular and energy distributions of the scattered intensity, it can be used as a weighting function to determine the average

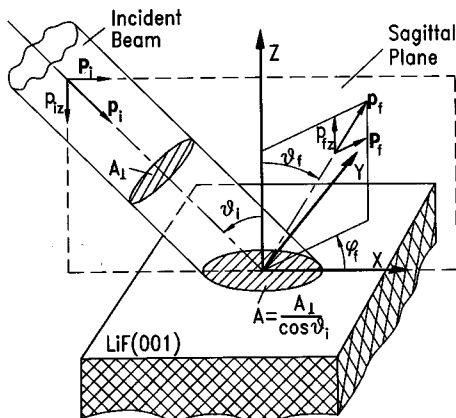


FIG. 4. Schematic diagram of the coordinate system showing the position of the beam and the relation of the beam cross section to the illuminated spot on the surface. The vector quantities and angles indicated are defined in the text.

properties of the scattered flux. For example, the average final energy \overline{E}_f of a scattered particle is given by

$$\overline{E}_f = \frac{1}{N} \int_0^\infty dE_f E_f \int d\Omega_f \frac{dR(\mathbf{p}_f, \mathbf{p}_i)}{dE_f d\Omega_f}, \quad (2)$$

where N is given by the integrated total scattered intensity

$$N = \int_0^\infty dE_f \int d\Omega_f \frac{dR(\mathbf{p}_f, \mathbf{p}_i)}{dE_f d\Omega_f}. \quad (3)$$

Likewise, the average of the α th Cartesian component of the momentum of a scattered particle $\overline{p}_{f\alpha}$ is given by

$$\overline{p}_{f\alpha} = \frac{1}{N} \int_0^\infty dE_f \int d\Omega_f p_{f\alpha} \frac{dR(\mathbf{p}_f, \mathbf{p}_i)}{dE_f d\Omega_f}, \quad (4)$$

and higher moments of the energy, momentum, or other measurable quantities are obtained in a similar fashion.

B. Definitions of measured coefficients

The expressions for the energy and force (drag) coefficients of a monoenergetic incident beam can be expressed in terms of the average final energy and momentum. The energy (or heat) transfer coefficient C_h is defined as¹

$$C_h = \frac{\dot{Q}}{\frac{1}{2} \rho u^3 A} = \frac{\overline{E}_f - E_i}{E_i} \cos \theta_i, \quad (5)$$

where \dot{Q} is the rate of heat transfer to the surface, $u = |\mathbf{p}_i|/m$ is the incident atom speed, and $A = A_\perp / \cos \theta_i$ is the area subtended by the beam spot on the surface where A_\perp is the cross sectional area of the incident beam near the surface (see Fig. 4). An important measurable property of the energy transfer is the recovery temperature T_r which is defined as the surface temperature at which the heat transfer \dot{Q} goes to zero for a given incident beam momentum.

The tangential force coefficient C_t is given by¹

$$C_t = \frac{F_t}{\frac{1}{2} \rho u^2 A} = 2 \cos \theta_i \frac{P_i - \overline{P}_f}{|\mathbf{p}_i|}, \quad (6)$$

where P_i and P_f are the respective components of the parallel momenta lying in the plane defined by the incident beam and the normal to the surface (the sagittal plane). Similarly, F_t is the tangential force in the sagittal plane. An interesting special case is that of complete accommodation of the incident beam upon collision. In this case $P_f = 0$ and

$$C_t = \frac{F_t}{\frac{1}{2} \rho u^2 A} = 2 \cos \theta_i \sin \theta_i. \quad (7)$$

This is commonly known as the limit of hypersonic free molecular flow and complete accommodation.^{1,9}

The normal force coefficient C_n is defined by¹

$$C_n = \frac{F_n}{\frac{1}{2} \rho u^2 A} = 2 \cos \theta_i \frac{\overline{|p_{fz}|} + |p_{iz}|}{|\mathbf{p}_i|}, \quad (8)$$

where F_n is the normal component of the force exerted on the surface by the incident beam. An interesting special case

is that of purely elastic specular scattering from a perfectly reflecting flat mirror surface. In this case, $p_{fz} = -p_{iz} = -p_i \cos \theta_i$, leading to the simple result

$$C_n = 4 \cos^2 \theta_i. \quad (9)$$

To obtain the case of free molecular flow and complete accommodation with a surface at temperature T_S , one uses $\overline{p_{fz}} \rightarrow \langle p_{fz} \rangle = \sqrt{\pi m k_B T_S / 2}$, which is the value of the normal momentum of a gas leaving the surface at equilibrium (k_B is Boltzmann's constant).

Other force coefficients which are of interest are the drag coefficient C_D , which measures the average force D exerted on the surface in the direction of the incident beam

$$C_D = \frac{D}{\frac{1}{2} \rho u^2 A} = 2 \cos \theta_i \left[1 - \frac{(\overline{\mathbf{p}_f \cdot \mathbf{p}_i})}{p_i^2} \right], \quad (10)$$

and the lift coefficient, which measures the magnitude of the force L perpendicular to the incident beam

$$C_L = \frac{L}{\frac{1}{2} \rho u^2 A} = 2 \cos \theta_i \frac{|\mathbf{p}_f \times \mathbf{p}_i|}{p_i^2}. \quad (11)$$

In some cases it is convenient to describe the energy and momentum exchange in terms of accommodation coefficients. For example, the energy accommodation coefficient for a monoenergetic incident beam may be defined by

$$\sigma_E(E_i) = \frac{\overline{E_f} - E_i}{\langle E_f \rangle - E_i} = \frac{\overline{E_f} - E_i}{2k_B T_S - E_i}, \quad (12)$$

where the notation $\langle E_f \rangle$ implies the average energy of an atom leaving the surface in equilibrium with the surface at temperature T_S . This definition is in analogy with the energy accommodation coefficient defined for the boundary between a surface at temperature T_S in contact with an ideal gas at temperature T_G . This accommodation coefficient is given by

$$\alpha_E(T_S, T_G) = \frac{\overline{E_f} - \langle E_i \rangle}{\langle E_f \rangle - \langle E_i \rangle} = \frac{\overline{E_f} - 2k_B T_G}{2k_B T_S - 2k_B T_G}. \quad (13)$$

The equilibrium accommodation coefficient $\alpha_E(T)$ is obtained in the limit of equal surface and gas temperatures. The monoenergetic incident beam coefficient $\sigma_E(E_i)$ has a distinct disadvantage in that it will normally become undefined for the surface temperature at which its denominator vanishes. Despite this inconvenience, $\sigma_E(E_i)$ is often useful as a measure of energy transfer between a beam and a surface.^{42,43} On the other hand, the accommodation coefficient $\alpha_E(T_S, T_G)$ remains well defined at all temperatures because the numerator and denominator both vanish linearly when $T_S \rightarrow T_G$, i.e., in this limit the average final energy $\overline{E_f}$ differs from $\langle E_i \rangle = 2k_B T_G$ only by a term which is linear in $T_S - T_G$.

In analogy to the energy accommodation coefficients defined above, a normal momentum accommodation coefficient η_N and a tangential momentum accommodation coefficient η_T ¹ are given by

$$\eta_N = \frac{|\overline{p_{fz}}| - |p_{iz}|}{\langle p_{fz} \rangle - |p_{iz}|} = \frac{|\overline{p_{fz}}| - p_i \cos \theta_i}{\sqrt{\pi m k_B T_S / 2} - p_i \cos \theta_i}, \quad (14)$$

and

$$\eta_T = \frac{\overline{P_i - P_f}}{P_i}, \quad (15)$$

where it is understood that $\overline{P_f}$ and P_i are the respective surface-parallel components in the sagittal plane. For the case of nonisotropic crystal surfaces, a transverse tangential momentum coefficient η_{TT} is

$$\eta_{TT} = \frac{\overline{P_{fT}}}{P_i}, \quad (16)$$

where $\overline{P_{fT}}$ is the average final parallel momentum perpendicular to the sagittal plane. The tangential momentum accommodation coefficients have the advantage that they are always well defined for all surface temperatures, unlike σ_E and η_N .

C. Scattering theory

As explained in Sec. III A all calculations depend on the microscopic differential reflection coefficient. Ideally, a full quantum mechanical multiphonon calculation is required, but since this is an exceedingly lengthy computational problem a simpler approach is developed. The total differential reflection coefficient is written as a summation of two terms, an elastic diffraction part, and a second part describing inelastic scattering about each of the diffraction peaks. A complete examination of the general multiphonon intensity as outlined in Appendix A shows that such an inelastic "foot" at the base of each diffraction peak is expected.²⁵ This model has the advantage that it accounts for the large diffraction peaks expected for highly corrugated surfaces and that each diffraction peak acts as the "generator" of an inelastic intensity lobe which surrounds it, yet the model is sufficiently tractable computationally to enable straightforward numerical calculations. In this model the diffraction is described by the exact quantum mechanical expression and the inelastic scattering about each peak is approximated by a semiclassical expression. However, the model goes over readily to the purely classical scattering case, either for a smooth crystal-line surface or for a rough surface, by taking the appropriate and easily effected limits.

A properly normalized differential reflection coefficient for this model is given by combining the elastic and inelastic contributions in the following manner:

$$\frac{dR^M}{d\Omega_f dE_f} = \frac{1}{N^{\text{el}}(T_S=0)} \frac{dR^{\text{el}}}{d\Omega_f dE_f} + \left(1 - \frac{N^{\text{el}}(T_S)}{N^{\text{el}}(T_S=0)} \right) \frac{1}{N^{\text{in}}(T_S)} \frac{dR^{\text{in}}}{d\Omega_f dE_f}, \quad (17)$$

where $dR^{\text{el}}/d\Omega_f dE_f$ is the purely elastic differential reflection coefficient including diffraction, $dR^{\text{in}}/d\Omega_f dE_f$ is the inelastic differential reflection coefficient, and their respective normalizations are $N^{\text{el}}(T_S)$ and $N^{\text{in}}(T_S)$. Expressions for these differential reflection coefficients are described below. Equation (17) for the overall differential reflection coefficient now contains both the elastic diffraction intensity of a

given peak intensity and the inelastic intensity associated with it, and in addition is normalized to unity.

The exact differential reflection coefficient for elastic diffraction is developed in Appendix A and is given by

$$\frac{dR^{\text{el}}}{d\Omega_f dE_f} = \sum_{\mathbf{G}} \frac{m^2 |\mathbf{p}_f|}{\hbar^4 p_{iz}} |\tau_{fi}^{\text{el}}(\mathbf{G})|^2 e^{-2W(\mathbf{p}_f, \mathbf{p}_i)} \times \delta(\mathbf{P}_f - \mathbf{P}_i - \hbar \mathbf{G}) \delta(E_f - E_i), \quad (18)$$

where \mathbf{G} is a reciprocal lattice vector of the surface lattice and $\tau_{fi}^{\text{el}}(\mathbf{G})$ is the exact transition matrix element for scattering by a surface potential which is periodic in two dimensions. The Dirac delta functions assure the conservation of energy in the incident and scattered beams and that the parallel momentum transfer satisfies the two-dimensional Bragg diffraction conditions. The normalization coefficient of the elastic differential reflection coefficient of Eq. (18), as given by the normalization Eq. (3), is temperature dependent and will be denoted by $N^{\text{el}} = N^{\text{el}}(T_S)$. The temperature dependence of this normalization coefficient comes entirely from the presence of the Debye–Waller factor $\exp[-2W(\mathbf{p}_f, \mathbf{p}_i)]$ in Eq. (18). The explicit model used in this paper for calculations of the elastic intensity will be elaborated below.

The inelastic differential coefficient is based on the extreme semiclassical expression of Eq. (45) which is derived in Appendix A. The development of $dR^{\text{in}}/d\Omega_f dE_f$ begins by considering a projectile colliding with a continuous vibrating surface at temperature T_S . The scattering intensity can be written analytically in closed form and is a Gaussian-like expression in parallel momentum exchange $\mathbf{P} = \mathbf{P}_f - \mathbf{P}_i$ and in the energy exchange $\Delta E = E_f - E_i$,^{25,44}

$$\frac{dR^{\text{in}}}{d\Omega_f dE_f} = \frac{m^2 v_R^2 |\mathbf{p}_f|}{4\pi^3 \hbar^2 p_{iz} S_{\text{u.c.}}} |\tau_{fi}|^2 \left(\frac{\pi}{\Delta E_0 k_B T_S} \right)^{3/2} \times \exp \left\{ - \frac{(\Delta E + \Delta E_0)^2 + 2v_R^2 \mathbf{P}^2}{4k_B T_S \Delta E_0} \right\}, \quad (19)$$

where v_R is a characteristic velocity of sound parallel to the surface, $S_{\text{u.c.}}$ is the area of a surface unit cell, \hbar is Planck's constant, and $|\tau_{fi}|^2$ is the scattering form factor of a surface unit cell. Although Eq. (19) appears to be a Gaussian-like function of energy and parallel momentum exchange, it is highly skewed on the energy gain side because of the energy dependence of the classical recoil energy transfer ΔE_0 given by

$$\Delta E_0 = (\mathbf{p}_f - \mathbf{p}_i)^2 / 2M. \quad (20)$$

The functional form of Eq. (19) is identical for any realistic continuum distribution of vibrational modes, thus the only dependence on the phonon model is through the characteristic velocity v_R which is a weighted average of phonon velocities parallel to the surface.⁴⁴ For perfectly ordered surfaces, the value of v_R is expected to be of the order of the Rayleigh velocity of sound.

The remaining quantity to be specified is the appropriate approximation for the form factor $|\tau_{fi}|^2$. An expression which has been extremely useful, both for multiphonon scattering^{25,45} and for single phonon studies,^{46,47} is a form

given by the distorted wave Born approximation,⁴⁶ namely the product of a Jackson–Mott matrix element v_{J-M} and a cutoff factor in parallel momentum given by

$$|\tau_{fi}|^2 = \exp(-P^2/\hbar^2 Q_c^2) |v_{J-M}(p_{fz}, p_{iz})|^2. \quad (21)$$

The cutoff factor $\exp(-P^2/\hbar^2 Q_c^2)$ is an approximation to the effects on the scattering matrix element due to corrugation of the surface potential in directions parallel to the surface.⁴⁶ The cutoff wave vector Q_c is the inverse of the correlation length on the surface for inelastic scattering. Q_c can be expressed as a cutoff momentum through the relation $P_c = \hbar Q_c$, has values for metal surfaces of $Q_c \approx 1 - 2 \text{ \AA}^{-1}$ as determined by single phonon intensity measurements,^{46,47} while for alkali halides it is considerably larger.^{19,20,48} For multiphonon studies, Q_c has been found to be somewhat larger than for single phonon intensities.^{25,47}

The Jackson–Mott matrix element is the matrix element of an exponentially repulsive surface potential

$$V^0(z) = v_0 e^{-\beta z}, \quad (22)$$

taken with respect to its own distorted Schrödinger equation eigenstates. It depends on only the perpendicular components of the momentum. Defining $q_i = p_{iz}/\hbar\beta$ and $q_f = p_{fz}/\hbar\beta$, it is given by⁷

$$v_{J-M}(p_{fz}, p_{iz}) = \frac{\hbar^2 \beta^2}{m} \frac{\pi^2 q_i q_f (q_f^2 - q_i^2)}{\cosh(\pi q_f) - \cosh(\pi q_i)} \times \left(\frac{\sinh(\pi q_f) \sinh(\pi q_i)}{\pi^2 q_f q_i} \right)^{1/2}. \quad (23)$$

The diagonal elements have a simple limiting form $v_{J-M}(p_{fz}, p_{fz}) = 2p_{fz}^2/m$. For elastic diffraction and single phonon inelastic scattering from metal surfaces, β is usually found to have values in the range of $2 - 3 \text{ \AA}^{-1}$.⁴⁷ From fits of elastic scattering from insulators such as alkali halides, the repulsive potential is found to be more rigid with range parameters of the order $\beta \approx 3 \text{ \AA}^{-1}$.²⁰ For multiphonon scattering under more semiclassical scattering conditions it is found empirically that β can be as large as $5 - 6 \text{ \AA}^{-1}$.⁴⁷ In the limit of a very hard repulsive surface, $\beta \rightarrow \infty$, the Jackson–Mott matrix element becomes

$$v_{J-M}(p_{fz}, p_{iz}) \rightarrow 2p_{fz} p_{iz} / m, \quad (24)$$

which is also the result obtained for an infinitely hard repulsive wall.

Contributions due to diffraction can now be readily included by modifying the inelastic differential reflection coefficient of Eq. (19). This model assumes an inelastically scattered lobe associated with each of the diffraction peaks, and that these inelastic lobes can be approximated by a semiclassical expression such as Eq. (19) but with its momentum shifted to correspond to the relevant diffraction peak,

$$\frac{dR^{\text{in}}}{d\Omega_f dE_f} = \frac{m^2 v_R^2 |\mathbf{p}_f|}{4\pi^3 \hbar^2 p_{iz} S_{\text{u.c.}}} \sum_{\mathbf{G}} |\tau_{fi}^{\text{in}}(\mathbf{G})|^2 \left(\frac{\pi}{\Delta E_{\mathbf{G}} k_B T} \right)^{3/2} \times \exp \left\{ - \frac{(\Delta E + \Delta E_{\mathbf{G}})^2 + 2v_R^2 (\mathbf{P} + \hbar \mathbf{G})^2}{4k_B T \Delta E_{\mathbf{G}}} \right\}, \quad (25)$$

TABLE I. Tables of the various scattering models used for calculations in this paper.

| Model | Description |
|---------------------------|---|
| Multilobe model | Equation (17), together with the elastic scattering amplitudes of Eq. (30), defines the complete dynamical model for inelastic scattering with diffraction. |
| Rough corrugation model | Same as multilobe model, but with a very large corrugation amplitude. |
| Single-lobe semiclassical | Only the specular peak lobe is retained from the multilobe model of Eq. (17). All other diffraction peak lobes are eliminated. |
| Single-lobe classical | Uses the classical expression of Eq. (19) for the differential reflection coefficient. |
| Classical rough surface | Single-lobe classical model with form factor equal to a constant. |
| Classical hard wall | Single-lobe classical model with hardwall form factor of Eq. (24). |
| Elastic diffraction | Uses the elastic diffraction differential reflection coefficient of Eq. (18) and the eikonal diffraction model of Sec. III C. |

where the scattering amplitudes are given by

$$\tau_{fi}^{\text{in}}(\mathbf{G}) = \tau_{fi}^{\text{el}}(\mathbf{G}) \frac{v_{M-J}(p_{fz}, p_{Gz})}{v_{M-J}(p_{Gz}, p_{Gz})} \times \exp\{-(\mathbf{P} + \hbar\mathbf{G})^2/2\hbar^2 Q_c^2\}. \quad (26)$$

$\tau_{fi}^{\text{el}}(\mathbf{G})$ is the elastic-limit scattering amplitude appearing in the diffraction intensity of Eq. (18) and is further specified below. The normal momenta of the diffraction peaks p_{Gz} appearing in Eqs. (25) and (26) are given by the momentum transfer in the diffraction process $\mathbf{p}_G = (\mathbf{P}_i + \hbar\mathbf{G}, p_{Gz})$ and by conservation of energy

$$p_{Gz}^2 = p_i^2 - (\mathbf{P}_i + \hbar\mathbf{G})^2. \quad (27)$$

The inelastic differential reflection coefficient of Eq. (25) has a temperature dependent normalization which is denoted by $N^{\text{in}}(T_S)$, and again this is determined as in Eq. (3).

The final remaining task is to choose the elastic diffraction amplitudes $\tau_{fi}^{\text{el}}(\mathbf{G})$. For this, a model which has been successfully used to describe the diffraction intensities observed in He/LiF scattering is employed.^{17,18} The cleaved LiF(001) surface presents square unit cells with sides of length a formed by the dominant corrugation of the F atoms.⁴⁹ The potential for the elastic scattering is taken as a repulsive hard wall at the position $z = \xi(x, y)$ with the corrugation function given by

$$\xi(x, y) = A \left[\cos\left(\frac{2\pi x}{a}\right) + \cos\left(\frac{2\pi y}{a}\right) \right], \quad (28)$$

and consequently the reciprocal lattice vectors are given by

$$\mathbf{G} = \mathbf{G}_{nm} = \left(\frac{2\pi n}{a}, \frac{2\pi m}{a} \right), \quad (29)$$

when m and n are integers.

For this hard wall model of the elastic He-LiF potential, the transition matrix amplitudes of the diffraction peaks can be calculated analytically using the semiclassical eikonal approximation,¹⁸ and the result for the relative amplitudes is given by

$$\tau_{fi}^{\text{el}}(\mathbf{G}_{nm}) = (-i)^{|m|+|n|} \frac{1 + \cos(\theta_i + \theta_G)}{\cos \theta_G (\cos \theta_i + \cos \theta_G)} \times J_{|m|}(\Delta \tilde{p}_{Gz} A / \hbar) J_{|n|}(\Delta \tilde{p}_{Gz} A / \hbar), \quad (30)$$

where θ_G is the polar angle of the diffraction beam associated with the reciprocal lattice vector \mathbf{G}_{nm} , and the perpendicular momentum exchange $\Delta \tilde{p}_{Gz} = |\tilde{p}_{iz}| + |\tilde{p}_{Gz}|$ is denoted by a tilde in order to indicate that in this diffraction model it is calculated with the inclusion of the semiclassical effect of the attractive physisorption well of depth ε . Equation (27) then becomes

$$\tilde{p}_{Gz}^2 = p_i^2 - (\mathbf{P}_i + \hbar\mathbf{G})^2 + 2m\varepsilon. \quad (31)$$

Equation (17), together with the elastic scattering amplitudes of Eq. (30), defines the complete multilobe model for dynamic inelastic scattering with diffraction.

In the course of this work several approximations to this multilobe model, listed in Table I in order of greater simplification, were used. The multilobe model differential reflection coefficient of Eq. (17) can be reduced to a single-lobe semiclassical model in the limit in which only the specular peak is retained and all other diffraction peaks are given zero scattering amplitude. Another important and useful limiting case is the classical limit of the single-lobe model which is used extensively below. The single-lobe classical limit has no diffraction and uses the classical expression of Eq. (19) for the differential reflection coefficient. The single-lobe semiclassical limit described above goes over into the single-lobe classical limit when the Debye–Waller factor becomes negligibly small, which will occur when the temperature or incident energy is sufficiently large.

The classical model can be made to correspond to a smooth crystalline surface or to a rough surface by an appropriate choice of the form factor. The classical hard wall limit is obtained when the inelastic form factor $|\tau_{fi}|^2$ is given by the square of the classical hard wall limit of the Jackson–Mott matrix element Eq. (24). Various rough-surface limits are obtained with different choices of the form factor. A convenient model for a rough surface which is utilized below

assumes that each unit cell of the surface is a hemisphere which scatters incoherently and uniformly in all directions. The form factor corresponding to this rough-surface limit is simply a constant and this will be called the classical rough-surface model. Especially for the force coefficients, it is of some interest to carry out calculations in the purely elastic diffraction limit. This can be accomplished by using as the (unnormalized) differential reflection coefficient the first term on the right-hand side of Eq. (17).

IV. COMPARISONS OF EXPERIMENT WITH THEORY

In the experiments, the surface temperatures were varied from 300 to 720 K and the incident angles ranged from normal incidence $\theta_i=0$ to $\theta_i=30^\circ$. Heat transfer coefficients C_h were measured as a function of surface temperature T_S at three incident angles, $\theta_i=0, 15,$ and 30° . The incident atom beam source was always held at a temperature of 300 K, which corresponds to a most probable beam energy of $E_i=63$ meV. Measurements of the normal and tangential force coefficients as a function of temperature were made simultaneously with the heat transfer coefficient measurements. Additionally, C_n and C_t were measured at a fixed surface temperature as a function of incident angle. The most extensive measurements were for a surface temperature $T_S=720$ K.

The validity of the classical versus the quantum mechanical theory can be estimated by evaluating the Debye–Waller factor $\exp(-2W)$ of Eq. (41) since the argument of the Debye–Waller factor is equal to the average number of phonons transferred in a given collision. For normal incidence at 63 meV and assuming the bulk Debye temperature of 730 K, Eq. (43) gives the conservative lower limit $2W \approx 2$ for a room temperature surface, which is smaller than the value $2W > 4-6$ for which the purely classical model becomes valid.⁵¹ Clearly, some aspects of quantum effects must be retained and it is for this reason that the semiclassical multilobe model which includes diffraction effects was developed.

A. Potential parameters for the He–LiF interaction

It is well established that He scattering from LiF at room temperature conditions exhibits the distinctly quantum mechanical features of diffraction and single phonon peaks,^{17,49} and this is why initial comparisons were made with the multilobe model. The full multilobe model used the best-fit parameters $\beta=9 \text{ \AA}^{-1}$, $Q_c=4.0 \text{ \AA}^{-1}$, $v_R=2000$ m/s, the corrugation parameter $A=0.065 \text{ \AA}$, and well depth $\epsilon=5$ meV. The He–LiF potential parameters used, as well as some other selected physical parameters for LiF, are listed in Table II.

The values of β and Q_c are somewhat larger, but consistent with other values obtained for scattering of He from LiF^{19,20} and for other insulator surfaces.^{48,51} A previous multiphonon study of He scattering from LiF(001) at a somewhat lower incident beam energy of 32 meV ($T_0=140$ K),¹⁹ based on a quantum mechanical version of the same theory used here, obtained values of $\beta=6$ and $Q_c=4.5 \text{ \AA}^{-1}$ which are not far from those used in Fig. 5. TOF He scattering experiments on other insulator surfaces such as KCN(001) have been fit with the large values $\beta=7.5$ and $Q_c=5.5 \text{ \AA}^{-1}$,⁵² and previous less extensive measurements on

TABLE II. Selected physical constants for LiF and best fit potential parameters used for the He–LiF(001) potential in the present calculations and comparisons with experimental data.

| Parameter | Description |
|--|-------------------------|
| $\beta=9.0 \text{ \AA}^{-1a}, 8.0 \text{ \AA}^{-1b}$ | Range parameter |
| $Q_c=4.0 \text{ \AA}^{-1a}, 4.5 \text{ \AA}^{-1b}$ | Cutoff parameter |
| $v_R=2000$ m/s ^{a,b} | Surface vibration speed |
| $\epsilon=5.0$ meV ^c | Well depth |
| $A=0.065 \text{ \AA}^a$ | Corrugation height |
| $a=2.84 \text{ \AA}^c$ | Lattice spacing |
| $\Theta_D=730$ K ^d | Bulk Debye temperature |

^aPresent work, multilobe model.

^bPresent work, single-lobe semiclassical model.

^cReference 17.

^dReference 69.

NaCl were fit with $\beta=5.6 \text{ \AA}^{-1}$ and a value of Q_c sufficiently large that the cutoff factor had no influence on the results.⁴⁸ Again, these parameter values are in reasonable agreement with those obtained here. For comparison, a table of known values of these potential parameters for a number of different insulator and metal surfaces which have been measured with either multiphonon or single phonon experiments is shown in Table III.

A large value of β implies that the repulsive surface potential is stiff and short-ranged. A large Q_c implies very little attenuation of the scattering amplitude with increasing parallel momentum transfer. This is consistent with a hard

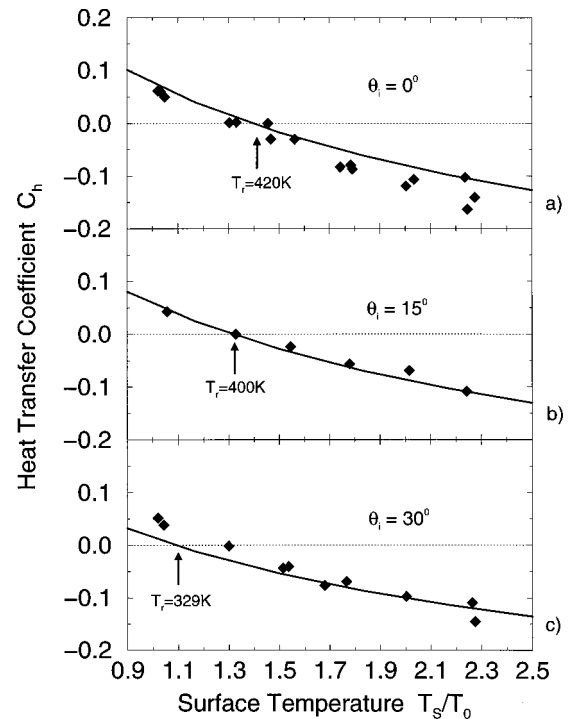


FIG. 5. Comparison of the measured data points (\blacklozenge) for the heat transfer coefficient C_h as a function of surface temperature T_S ($T_0=300$ K) with calculations using the full multilobe model for three different incident angles, (a) $\theta_i=0$, (b) $\theta_i=15$, and (c) $\theta_i=30^\circ$. The other parameters are $\beta=9 \text{ \AA}^{-1}$, $Q_c=4 \text{ \AA}^{-1}$, $v_R=2000$ m/s, $\epsilon=5$ meV, and $A=0.065 \text{ \AA}$.

TABLE III. Potential parameters β , Q_c , v_R , and effective Debye temperatures Θ_D obtained by fitting experimental data to theoretical calculations from both single and multiple phonon studies for several different metal and insulator surfaces. RW and LR signify values taken from studies of single phonon Rayleigh wave and longitudinal resonance modes, respectively, and multi signifies from multiphonon studies.

| Insulators | Direction | Mode | $\beta[\text{\AA}^{-1}]$ | $Q_c[\text{\AA}^{-1}]$ | $\theta_D[\text{K}]$ | $v_R[\text{m/s}]$ |
|------------|--|-------|--------------------------|------------------------|----------------------|-------------------|
| LiF(001) | ... | Multi | 9.0 ^a | 4.0 ^a | ... | 2000 ^a |
| LiF(001) | ... | Multi | 8.0 ^b | 4.5 ^b | ... | 2000 ^b |
| LiF(001) | $\langle 110 \rangle$ | RW | ... | ... | ... | 4060 ^c |
| LiF(001) | $\langle 100 \rangle$ | RW | ... | ... | ... | 3897 ^c |
| LiF(001) | $\langle 100 \rangle$ | Multi | 6.0 ^d | 4.5 ^d | 520 ^d | ... |
| KCN(001) | $\langle 100 \rangle, \langle 110 \rangle$ | Multi | 7.5 ^e | 5.5 ^e | 123 ^e | ... |
| NaCl(001) | $\langle 100 \rangle$ | Multi | 5.6 ^f | $>10^f$ | 270 ^f | ... |
| Metals | | | | | | |
| Cu(001) | $\langle 100 \rangle, \langle 110 \rangle$ | Multi | 5.7 ^g | 2.4 ^g | 270 ^g | 3000 ^g |
| Cu(001) | $\langle 100 \rangle, \langle 110 \rangle$ | Multi | 2.9 ^h | 1.0 ^h | 270 ^h | ... |
| Cu(001) | $\langle 100 \rangle$ | RW | 3.0 ⁱ | 1.0 ⁱ | 267 ⁱ | ... |
| Cu(001) | $\langle 100 \rangle$ | LR | 5.0 ⁱ | 1.32 ⁱ | 267 ⁱ | ... |
| Cu(001) | $\langle 110 \rangle$ | RW | 4.67 ⁱ | 1.28 ⁱ | 267 ⁱ | ... |
| Cu(001) | $\langle 110 \rangle$ | LR | 3.35 ⁱ | 1.08 ⁱ | 267 ⁱ | ... |
| Cu(001) | $\langle 100 \rangle$ | RW | 2.1 ^j | 0.95 ^j | 230 ^k | ... |
| | | | | | 280 ^l | ... |
| Ag(001) | $\langle 100 \rangle$ | RW | 2.77 ^m | 0.87 ^m | 253 ⁿ | ... |
| Ag(001) | $\langle 100 \rangle$ | LR | 5.30 ^m | 1.20 ^m | 253 ⁿ | ... |
| Ag(001) | $\langle 110 \rangle$ | RW | 4.85 ^m | 1.15 ^m | 253 ⁿ | ... |
| Ag(001) | $\langle 110 \rangle$ | LR | 4.12 ^m | 1.06 ^m | 253 ⁿ | ... |
| Ag(111) | $\langle 11\bar{2} \rangle, \langle 110 \rangle$ | RW | 4.0 ^o | 0.74 ^o | 145 ^p | ... |
| Au(111) | $\langle 11\bar{2} \rangle, \langle 110 \rangle$ | RW | 2.10 ^q | 0.74 ^q | ... | ... |
| Rh(111) | $\langle 11\bar{2} \rangle, \langle 110 \rangle$ | RW | 3.15 ^r | 0.82 ^r | 255 ^s | ... |
| Pt(111) | $\langle 11\bar{2} \rangle, \langle 110 \rangle$ | RW | ... | 0.57 ^t | 111 ^u | ... |
| Ni(110) | $\langle 100 \rangle$ | RW | 2.92 ^v | 0.84 ^v | 595 ⁿ | ... |
| Al(111) | $\langle 11\bar{2} \rangle, \langle 110 \rangle$ | RW | 4.0 ^w | 0.92 ^w | ... | ... |

^aPresent work, full diffraction model.

^bPresent work, single-lobe model.

^cReference 50.

^dReference 19.

^eReference 51.

^fReference 48.

^gReference 52.

^hReference 53.

ⁱReference 47.

^jReference 54.

^kReference 55.

^lReference 56.

^mReference 57.

ⁿReference 58.

^oReference 46.

^pReference 59.

^qReference 60.

^rReference 61.

^sReference 63.

^tReference 64.

^vReference 65.

^uReference 62.

^wReference 66.

repulsive potential and also with a rough surface in the sense of having a large corrugation which makes it easier to scatter projectiles out to large angles away from the specular beam. In the classical limit of very high incident projectile energies, one expects $\beta \rightarrow \infty$, $Q_c \rightarrow \infty$, and $v_R \rightarrow 0$.⁶⁷ Thus, these higher values of β and Q_c found here reflect not only the hardness of the LiF repulsive potential, but also indicate an approach toward the classical limit.

The parameter v_R is a weighted average of phonon velocities parallel to the surface,⁴⁴ and hence is expected to have a value somewhere in the neighborhood of the Rayleigh mode, which is the dominant surface-localized phonon. The value of $v_R = 2000$ m/s used for Fig. 5 can be compared to the measured Rayleigh mode velocities for LiF(001) of 3900 m/s in the $\langle 100 \rangle$ azimuth or 4060 m/s in the $\langle 110 \rangle$,⁵⁰ and also compares favorably with the Rayleigh velocity typical of metals; for example, a value of 1700 m/s which has been measured for the Cu(001) surface.⁶⁸ The remaining parameters in the theory are the well depth ϵ and the corrugation

parameter A needed for determining the diffraction peak intensities. These have been determined by Boato *et al.* through extensive comparisons with diffraction data to be $\epsilon = 5$ meV and $A = 0.145$ \AA .¹⁷ However, the independent diffraction measurements we have made on the current crystal sample produce weaker diffraction peak intensities²⁶ which we were able to better match using the eikonal approximation of Eq. (30) with a smaller corrugation amplitude of $A = 0.065$ \AA . An example of the comparison of our diffraction data with both corrugation parameters is shown in Fig. 3. For comparison, we show in Fig. 3, in addition to the calculations for $A = 0.065$, results for $A = 0.07$, $A = 0.085$, and $A = 0.145$ \AA . It is clear that the corrugation of $A = 0.145$ \AA shown in the square symbols in Fig. 3 overestimates the intensity of the higher order diffraction peaks measured on this sample. The value of $A = 0.065$ \AA most closely matches all the measured peaks. To demonstrate the sensitivity of the fit, the results for the slightly larger value of $A = 0.07$ \AA are also shown as circles, and although the first-order peaks are

somewhat better matched, the very weak second-order peaks are overestimated. The lattice parameter a is the distance between F ions on the (001) surface which is $a = 2.84 \text{ \AA}$. Table II gives a compilation of all parameters used in the present calculations.

B. Heat transfer coefficients

Figure 5 shows the experimental data for the heat transfer coefficient, all taken with Knudsen number $K_{n0} \geq 4.3$, plotted as a function of the ratio of the surface temperature to the source temperature $T_0 = 300 \text{ K}$ for three different incident angles. The solid lines are the best-fit theoretical calculations for the full multilobe model of Eq. (17) using the parameters of Sec. IV A and Table II. From Fig. 5 it is clear that at low surface temperatures C_h is positive, implying that the beam gives up heat to the surface, while at higher T_S the surface gives energy up to the beam and C_h is negative. The theoretical curve has a pronounced negative curvature which agrees rather well with the experimental points for all three incident angles. The surface temperature for which C_h vanishes is the recovery temperature T_r for which no heat is transferred between the surface and the beam. The recovery temperature is observed to decrease with increasing incident polar angle, also in good agreement with theory.

The angular dependence of the recovery temperature T_r , as well as the distinct curvature of the C_h vs T_S results are interesting because both are at variance with simple accommodation coefficient theory. This is readily seen from the accommodation coefficient expression of Eq. (12), which when combined with the definition of C_h in Eq. (5) gives

$$C_h = \sigma_E \frac{2k_B T_S - E_i}{E_i} \cos \theta_i. \quad (32)$$

The above expression for C_h is linear in T_S if σ_E is assumed to be constant, in contrast to the distinctly nonlinear behavior of the data. With the relation between the incident beam energy and the stagnation temperature T_0 of the jet beam source $E_i = 5k_B T_0/2$,¹ and setting $C_h = 0$ in (32), gives $T_r = 1.25T_0$, which is independent of the incident angle and the value of the accommodation coefficient. This is a poor approximation to the recovery temperature determined from the zero intercept of the theory curves in Fig. 6, which for $T_0 = 300 \text{ K}$ are $T_r = 420, 400,$ and 329 K for $\theta_i = 0, 15,$ and 30° , respectively. The decrease of T_r with increasing θ_i agrees with other experiments which show that energy losses depend predominantly on the energy associated with the normal motion of the incident particles, which becomes smaller with increasing polar angle.⁷⁰⁻⁷² Interestingly, the ratio of T_r at $\theta_i = 30$ and 0° is $329/420 = 0.78$, which is very near to the $\cos^2 30^\circ = 0.75$ corresponding to normal energy scaling.

At temperatures of $T_S > 500 \text{ K}$ where most measurements were made, the Debye-Waller exponent takes on values $2W > 4$ and the scattering can be well described by a classical theory. Figure 6 shows the same experimental data as in Fig. 5 but now compared with the single-lobe classical version of the theory with slightly modified best-fit parameters of $\beta = 8 \text{ \AA}^{-1}$, $Q_c = 4.5 \text{ \AA}^{-1}$, and $v_R = 2000 \text{ m/s}$. The general features of the single-lobe calculation in Fig. 6 are

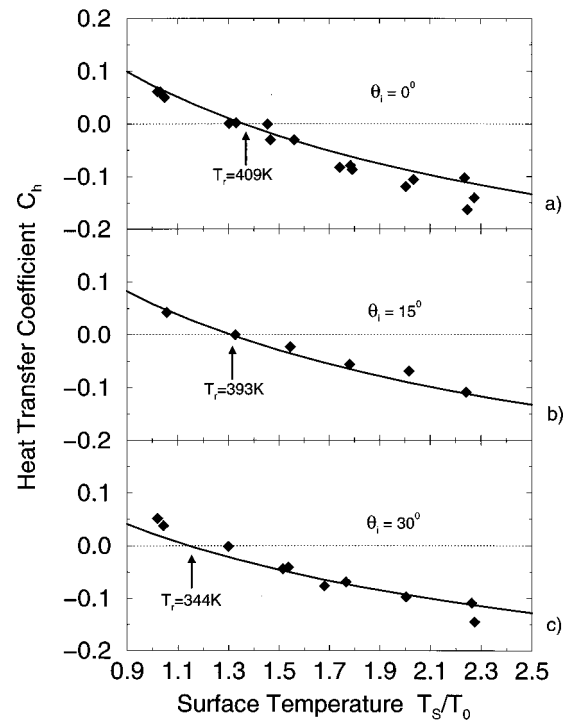


FIG. 6. Comparison of measured data points (\blacklozenge) for the heat transfer coefficient C_h as a function of surface temperature with the single-lobe classical model for three different incident angles: (a) $\theta_i = 0$, (b) 15 , and (c) 30° . The solid lines are calculated with $\beta = 8 \text{ \AA}^{-1}$, $Q_c = 4.5 \text{ \AA}^{-1}$, and $v_R = 2000 \text{ m/s}$.

quite similar to the full diffraction calculation in Fig. 5 and the fit to the data is nearly as good. The values of the recovery temperature, as determined from the zero intercept of the single-lobe theory curves in Fig. 6, are $T_r = 409, 393,$ and 344 K for $\theta_i = 0, 15,$ and 30° , respectively. In this case the calculations of T_r do not appear to scale directly with the normal energy $E_\perp = E_i \cos^2 \theta_i$. For example, the ratio of the T_r values for $\theta_i = 30$ and 0° is $344/409 = 0.84$, which compares more favorably with $\cos^2 30^\circ = 0.75$. However, the good overall fit obtained with the single-lobe classical theory shows that this simpler theory may be quite useful in explaining energy exchange. A table of the observed recovery temperatures and the calculated values for the three measured incident angles is presented in Table IV.

C. Force coefficients

The measured normal force coefficients as a function of θ_i and at a temperature $T_S = 720 \text{ K}$ are compared with the theoretical calculations of both the single-lobe classical

TABLE IV. Table of calculated and experimentally measured recovery temperatures T_r for the three measured incident angles.

| Incident angle θ_i | Experiment T_r (K) | Multilobe T_r (K) | Single-lobe classical T_r (K) |
|---------------------------|----------------------|---------------------|---------------------------------|
| 0° | 400 ± 20 | 420 | 409 |
| 15° | 398 ± 20 | 400 | 393 |
| 30° | 380 ± 20 | 329 | 344 |

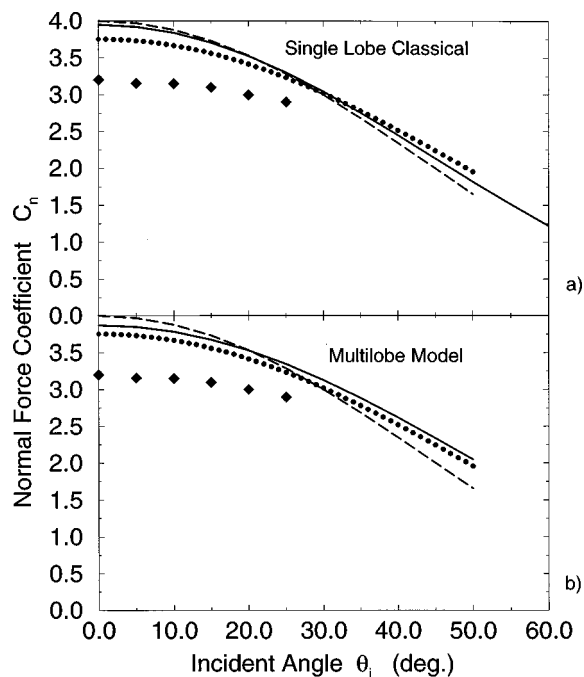


FIG. 7. Comparisons of the experimental points (\blacklozenge) for the normal force constant C_n as a function of the incident angle θ_i at a surface temperature of 720 K with the theoretical model calculations. The solid lines are the theoretical model calculations: (a) calculated with the single-lobe classical model using the same parameters as in Fig. 6, and (b) calculated with the full multilobe model using the same parameters as in Fig. 5. The dashed lines are the limiting case of specular reflection, the filled circles are the limiting case of complete accommodation and free molecular flow.

model and the multilobe model in Fig. 7. For neither of the two models is the theoretical agreement with the force coefficient data as good as it was for the heat transfer coefficient as a function of temperature. The multilobe model calculation comes somewhat closer to the experiment, but neither model is any better than the crude estimate of the limiting case of complete accommodation and free molecular flow. This discrepancy may originate from residual surface roughness as discussed in Sec. IV D below.

The measured tangential force coefficients C_t are shown in Fig. 8 as a plot similar to that for C_n in Fig. 7. Here the agreement of the calculations with the measurements is not at all good; in fact, both models predict very little parallel momentum transfer to the surface. There are some uncertainties in the data as indicated by the fact that the data do not tend to zero at normal incidence as expected, rather the data seem to have a finite interception point at $\theta_i = 0^\circ$. This may be partly explained by the estimated 5° uncertainty in the measurement of the incident angle and by the small cleavage planes at the edge of the crystal which were exposed to the incident beam at the larger incidence angles. However, the experimental uncertainties do not seem to explain the large discrepancy between the calculations and the data. Again, further calculations with very rough corrugated surfaces indicate that this discrepancy may be due to surface roughness as discussed in Sec. IV D below.

D. Rough corrugation results

Roughness such as adsorbates or defects, the most important of which in the present case is probably oil molecules

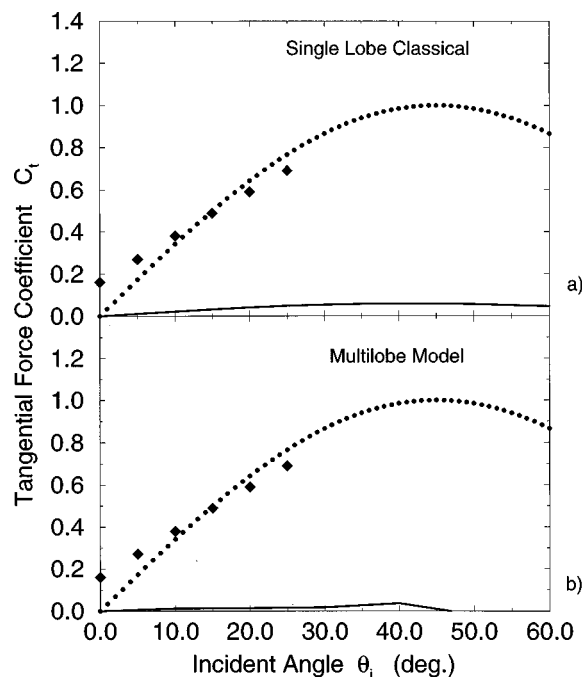


FIG. 8. Comparisons of the experimental points (\blacklozenge) for the tangential force coefficient C_t as a function of the incident angle θ_i at a surface temperature of 720 K with the theoretical model calculations. The solid lines are: (a) calculated with the single-lobe classical model with the same parameters as in Fig. 6, and (b) calculated with the full multilobe model using the same parameters as in Fig. 5. The filled circles are the limiting case of complete accommodation and free molecular flow.

or other contamination from the residual gas, breaks the translationally invariant symmetry of an otherwise ordered surface. Such symmetry breaking disorder opens new channels of scattering and/or facilitates scattering into channels which otherwise might have very weak intensities.^{12,13,16} One would expect that in the semiclassical scattering regime the total energy exchange would be less affected by roughness than the impulsive forces due to momentum exchange. By scattering projectiles into large angles away from the specular, disorder tends to lower the average final perpendicular momentum of a projectile, which according to Eq. (8) would reduce the normal force coefficient C_n and make the calculated curves of Fig. 7 come into better agreement with experiment. Similarly, roughness on the surface, especially the possibility of multilayer steps, would tend to enhance the parallel momentum transfer, making C_t larger, and this tendency would be greater at larger incident polar angles.

There are several simple ways in which roughness can be introduced into the theoretical model. The first, and most realistic, is to use the single-lobe classical model with a classical form factor. The classical single-lobe model is the limit in which each scattering center on the surface scatters independently, and all quantum interference has disappeared. This is the limit of a totally rough surface, although the degree of roughness is controlled by the shape of the form factor. Two of the many possible choices of form factors are interesting to examine. The first of these is a constant form factor which corresponds to hemispherical scattering centers on the surface which scatter uniformly in all momentum directions. This is the *classical rough-surface* model discussed

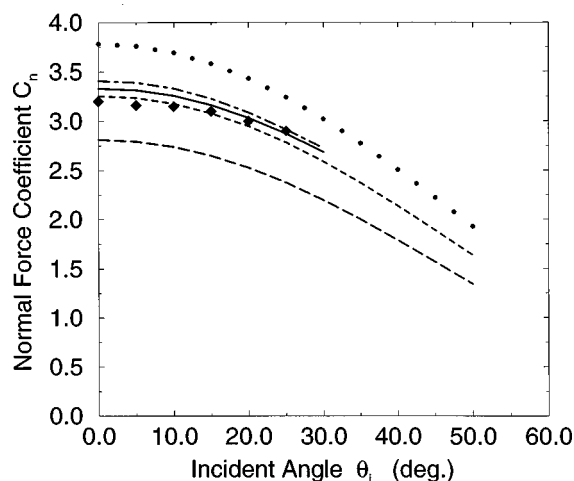


FIG. 9. Comparisons of the experimental points (\blacklozenge) of C_n vs θ_i ($T_S = 720$ K) with rough-surface calculations. The solid curve is for the rough corrugation model with a corrugation height $A = 0.25 \text{ \AA}$, and the dashed-dot curve is also for the rough corrugation model with $A = 0.5 \text{ \AA}$, using the full multilobe diffraction model as in Fig. 7, both with $\beta = 9 \text{ \AA}^{-1}$, $Q_c = 4.0 \text{ \AA}^{-1}$, and $v_R = 2000$ m/s. The dashed curve is the calculation using the classical rough-surface model for hard spheres scattering. The filled circles are the classical hard wall model. The short dashed line is the result for a surface with 42% of its area in an ordered state (calculated with the same parameters as in Fig. 5) and 58% covered with rough spherical impurities.

above in Sec. III C. The second choice of form factor is the *classical hard wall* limit of Eq. (24) in which $\beta = Q_c \rightarrow \infty$ and $v_R \rightarrow 0$.

A quite different approach is to simulate roughness by raising the corrugation to abnormally large values in the full diffraction model. This is called the *rough corrugation model*. Although this is a somewhat poor simulation of the randomness which is expected to accompany disorder, it is a simple method for enhancing the probability of scattering to very large angles away from the specular, which is a major effect of defects and roughness. These three models: the *classical rough-surface* model, the *classical hard wall model*, and the *rough corrugation model* will be used to discuss the effects of roughness on the force coefficients.

Figure 9 shows graphs of C_n calculated with all three of the above rough-surface models. The solid and dash-dot curves in Fig. 9 show graphs of C_n calculated with the *rough corrugation* (diffraction) model with the same potential parameters as Fig. 7 ($\beta = 9 \text{ \AA}^{-1}$, $Q_c = 4.0 \text{ \AA}^{-1}$, and $v_R = 2000$ m/s) but with two different enhanced values of the corrugation height, $A = 0.25$ and $A = 0.5 \text{ \AA}$, respectively. Both of these curves are now in reasonable agreement with the experimental points, lending credence to the idea that at least some of the discrepancy with experiment appearing in the clean surface calculations of Fig. 7 may be due to roughness on the surface of the LiF crystal sample. The curve of filled circles in Fig. 9 gives the result of a calculation with the *classical hard wall* model, and clearly gives results which are much larger than the measured values of C_n . Curiously, this is almost identical to the result given by the limiting case of complete accommodation and free molecular flow, and indicates that the surface is probably considerably rougher than the simple loss of quantum coherence embod-

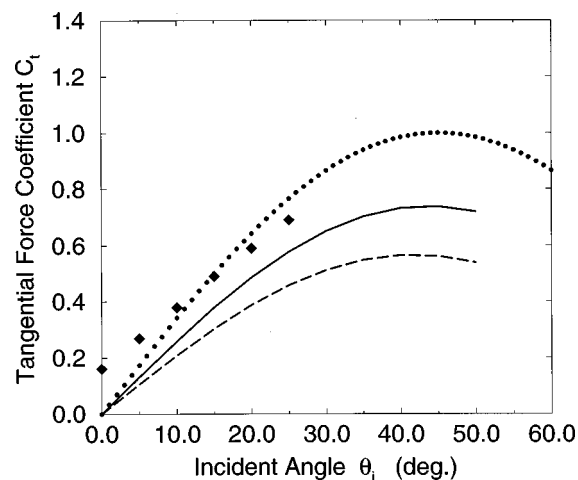


FIG. 10. Comparisons of experimental points (\blacklozenge) of C_t vs θ_i ($T_S = 720$ K) with the classical rough-surface model calculations. The solid line is for the classical hard wall model with $\beta = Q_c \rightarrow \infty$ and $v_R \rightarrow 0$. The dashed line is for the classical rough-surface collision model. The filled circles are the complete accommodation and free molecular flow limit.

ied in a classical hard wall. The long dashed curve in Fig. 9 shows the result of the calculation with the *classical rough-surface* model in which the form factor is a constant corresponding to hemispherical defects. This clearly overcompensates and predicts a normal force coefficient which is too small, and this indicates that the surface is not totally rough and incoherent as this model would imply.

A measure of the roughness of the surface is estimated by determining the fraction of the rough surface which is needed in order to come into agreement with the measured data. This is shown in the final curve in Fig. 9, the short-dashed line, which consists of the linear combination of 58% of the *classical rough-surface* (spherical hemisphere corrugation) model calculation, and 42% of the ordered *multilobe* surface diffraction model of Figs. 5 or 7. These calculations indicate that somewhat over half (58%) of the surface has to be made rough in order to arrive at agreement with the experimental data.

Similar calculations for the transverse force coefficient are shown in Fig. 10. The classical hard wall model is shown in the solid line and the rough spherical model is the dashed line. Interestingly, the classical hard wall model agrees somewhat more closely with the data than the spherical model, but both show a considerably larger tangential force than either of the two ordered surface models shown in Fig. 8. Considering the fact that the experimental uncertainty is the largest for these C_t measurements, both of these calculations can be considered in reasonable agreement with the experiment. In fact, a shift of the experimental points in the direction of larger incident angles by 5° , which is the estimated experimental uncertainty for this measurement, would bring the experiment in quite good agreement, especially with the classical hard wall calculation. The rough corrugated model calculations are not shown in Fig. 10 because they give results much too small, very similar to the single-lobe and multilobe model calculations of Fig. 8.

The calculations presented in Figs. 9 and 10 indicate the importance of roughness on the surface and the need for

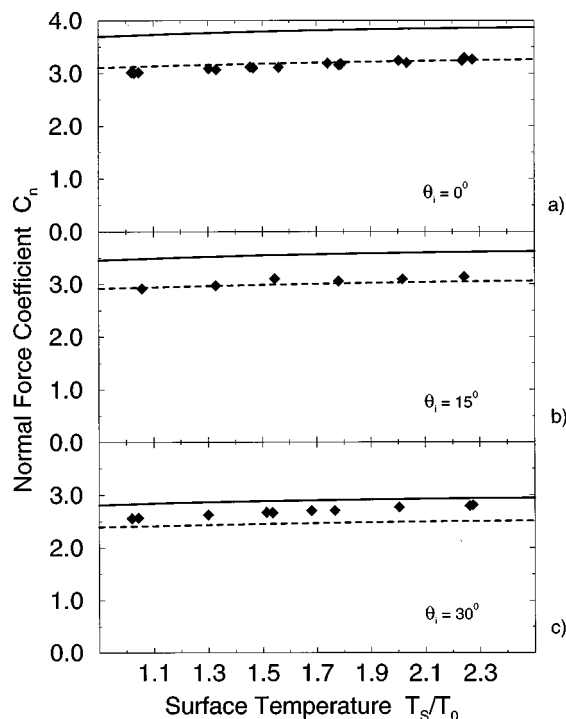


FIG. 11. Comparisons of experimental points (\blacklozenge) at $T_0=300$ K with calculations for the normal force coefficient C_n as a function of surface temperature for the three different incident angles: (a) $\theta_i=0^\circ$, (b) $\theta_i=15^\circ$, and (c) $\theta_i=30^\circ$. The calculations shown as solid lines are with the full multilobe model using the same best-fit parameters as for Fig. 5. The short-dashed curves are the linear combination of the solid line calculation and the classical rough-surface calculation simulating an ordered surface partially covered with a rough layer in the proportion 42%/58%, respectively, as in Fig. 9.

carefully monitoring the state of surface disorder in such experiments. These calculations indicate that a small amount of high profile residual disorder created in the preparation of the crystal face, or due to contamination of the crystal, could account for the discrepancies between the experimentally measured force coefficient values and the ordered surface calculations.

E. Dependence of the force-coefficients on surface temperature

The dependence of the tangential and normal force coefficients on surface temperature was measured simultaneously with the heat transfer coefficients discussed in Sec. IV B. In Fig. 11 the normal force coefficients are plotted as a function of surface temperature for the three different incident angles. The data are compared to the calculations with the full multilobe model using the best-fit parameters of Fig. 5. Just as in the angular dependence shown in Fig. 7(b), the calculations using parameters that give the best fit with the data for C_h shown in Fig. 5 overestimate the value of the normal force constant at all measured angles. There is very little temperature dependence exhibited by the data, and the calculations show similar behavior. The excellent agreement between the slopes of the two curves shows that the temperature dependence is well predicted by the theory. The calculation shown by short-dashed curves in Fig. 11 is the same as in Fig. 9: 48% of the surface is ordered and the intensity

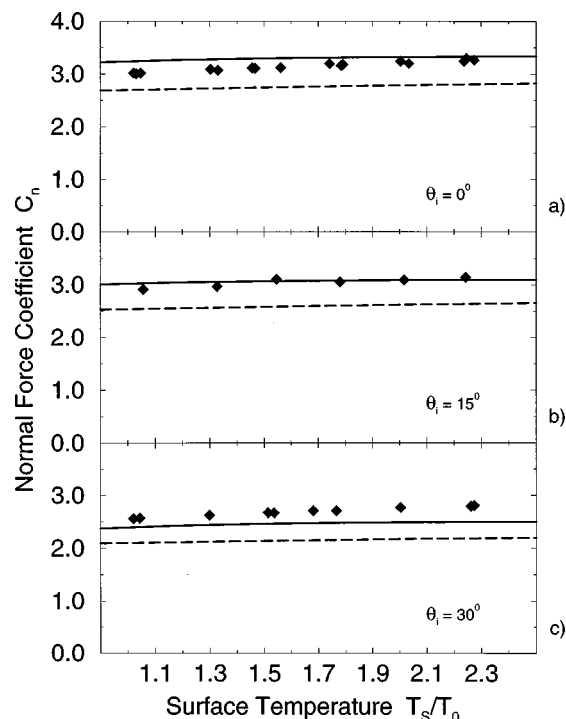


FIG. 12. Comparison of experimental points (\blacklozenge) at $T_0=300$ K with calculations of the normal force coefficient C_n as a function of surface temperature as in Fig. 11. The calculations shown as solid lines are with the full diffraction rough corrugation model with the (rough-surface) corrugation height of 0.25 \AA , and the dashed lines are the classical rough-surface model calculations, as in Fig. 9.

from that part is calculated with the same best-fit parameters as the solid curve; the remaining 58% of the surface is rough and its intensity is calculated with the classical rough-surface model.

Figure 12 compares the same data to the calculations of the full diffraction model but with the rough corrugated surface (i.e., the rough corrugation model) with a corrugation height of 0.25 \AA which gave rather good agreement with the angular dependence in Fig. 9. Again, as in Fig. 11, the temperature dependence predicted by the theory agrees with the experiment, but in addition the actual magnitudes of C_n are also reasonably well matched. The dashed line in Fig. 12 shows the calculations for the classical rough-surface model. This reasonable agreement with the experiment shown by both of these calculations is taken as additional evidence that there may be some residual roughness on the experimental samples which has contributed to reducing the C_n values from those expected for a perfectly ordered surface.

Figure 13 shows the measured temperature dependence of the tangential force coefficient as a function of surface temperature for three different incident angles. C_t increases with increasing θ_i , but for all three measured angles is very nearly constant as a function of temperature. Calculations of C_t using either of the ordered surface models (the full multilobe model or the single-lobe classical model) also give virtually no dependence of C_t on surface temperature T_s , in agreement with the measurements, but the calculated magnitudes of C_t are much smaller than measured, as is evident from Fig. 8. Much better agreement is achieved with the

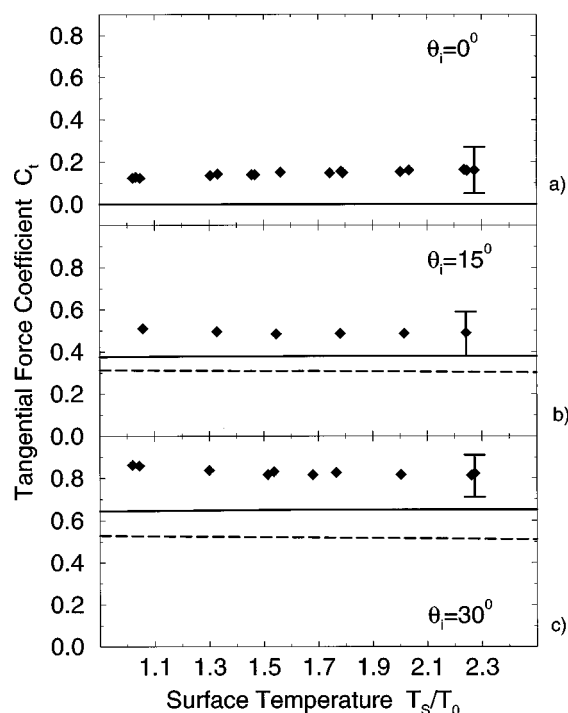


FIG. 13. Comparisons of experimental points (\blacklozenge) at $T_0 = 300$ K with calculations for the tangential force coefficient C_t as a function of surface temperature for the three different incident angles: (a) $\theta_i = 0^\circ$, (b) $\theta_i = 15^\circ$, and (c) $\theta_i = 30^\circ$. The calculations shown as solid lines are for the classical hard wall model, and the dashed lines are the results of the classical rough-surface model, as in Fig. 10. The error bars at the highest temperature data points indicate the range of values produced by an uncertainty of 5° in the incident angle, as determined from Fig. 10.

classical hard wall model using the rough-surface parameters of Fig. 10, which is shown as a solid line in Fig. 13. Clearly, the nearly constant temperature dependence of the measurements is correctly predicted by the calculations, but in addition the actual experimental and calculated magnitudes are in near agreement if one takes into account the error bars, also shown in Fig. 13, associated with a possible 5° uncertainty in the determination of the incident angle. Shown also in Fig. 13 as a dashed line is the calculation of C_t with the classical rough-surface model. This rough-surface calculation does not agree quite as well with the experimental data as the classical hard wall model, but the nearly constant temperature dependence is clearly apparent. Once again, this agreement with the rough-surface calculations is indicative that the rather large measured values of C_t may be due to a certain degree of inherent roughness present on the surface.

V. CONCLUSIONS

For the first time the energy and momentum transfer of gas atoms to a well defined crystal surface have been measured in a high vacuum wind tunnel environment. By using a directed beam of helium atoms with a large Knudsen number and a well defined velocity, with different specified angles of incidence on a clean freshly cleaved single crystal LiF(001) surface, conditions similar to those in high resolution scattering of atoms from surfaces are achieved. Despite the small beam fluxes and small size of the sample, it was possible to

measure the heat transfer and the forces exerted on the sample with considerable accuracy. These favorable conditions facilitated a detailed simulation of the measured transport properties using scattering theories which are well established and thoroughly developed through extensive comparisons with the recently available extensive high resolution elastic diffractive and one phonon inelastic scattering data.^{21,22} This latter work has provided a very detailed understanding of the interaction potential between gas atoms and single crystal surfaces, especially for He-LiF(001).^{17,18,21,22} For the present investigation this system also has additional advantages deriving from the inertness of He and its negligible sticking probability, as well as from the unusual inertness of the LiF(001) surface, which, for example, absorbs water, a major residual gas contaminant, only at temperatures below about 100 K. Thus by choosing this special gas-surface combination in the present combined experimental and theoretical investigation, the most favorable conditions for a direct comparison of microscopic scattering theories with a macroscopic gas-surface experiment have been achieved.

To describe these new experiments, a general scattering theory suitable for numerical simulations has been formulated. The theory is based on the semiclassical limit which has proven to be successful for describing high resolution scattering experiments. The theory not only gives the exact results for the scattered intensities in the extreme quantum mechanical limit of elastic diffraction but also becomes exact in the classical limit. Between these two limits it interpolates with semiclassical approximations. Two distinct theoretical models are presented, as well as several variations of these two models. The first is a near classical or single-lobe classical model which is valid at high incident energies, large surface temperatures, and for heavier mass projectile gases where no diffraction occurs. The second model is the semiclassical multilobe model which includes effects of quantum mechanical diffraction from ordered surfaces. These theories can easily be applied to a wide range of different gases and surface conditions.

The calculated average energies and momenta of gas atoms scattered from the surface are compared with the experimentally measured energy transfer coefficient and force coefficients. The good agreement between theory and experiment for the heat transfer coefficient indicates the validity of the most realistic multilobe model for calculating energy transfers in gas-surface interactions. The comparisons with the measured normal and tangential force coefficients, however, show large deviations. It is demonstrated that this can be interpreted as providing clear evidence for the presence of a significant amount of residual roughness on the surface. On the other hand, the HAS measurements made after the wind tunnel experiments produced angular distributions with sharp diffraction features and TOF distributions with sharp single phonon features (see Fig. 3) very similar to previous measurements on clean and ordered single crystal LiF.⁴⁹ The HAS experiments may indeed have had a much cleaner surface because of the substantially better vacuum and cleaner environment of the vacuum chamber. The discrepancy between the measured magnitudes of C_n and C_t

and the ordered surface calculations, as well as the differences between the HAS and the wind tunnel measurements, indicates the need in the future to even more carefully control the surface for roughness and disorder. The fact that the measurements of C_n and C_t were in much better agreement with the classical rough-surface model calculations may be indicative that the force coefficients are extremely sensitive to defects and disorder on the surface.

Several of the measured quantities which are in good agreement with the present theoretical model deviate significantly from the predictions of simple accommodation coefficient theory. In particular, the surface recovery temperature T_r at which there is no heat transfer between the beam and the surface is strongly dependent on the angle of incidence, whereas such a dependence is not predicted by a simple accommodation coefficient description. Moreover, the measured and calculated values of the recovery temperatures near normal incidence are much larger than the constant value predicted by the simple accommodation model. Furthermore, the accommodation coefficient model predicts a linear dependence of the normal force constant C_n on surface temperature in the region of the recovery temperature, in contradiction to the observed nonlinear dependence.

ACKNOWLEDGMENTS

We thank J. Lüdecke for carrying out the high resolution He atom scattering experiments which served to characterize the crystal surfaces after the wind tunnel experiments. We also gratefully acknowledge the skillful and patient assistance of G. von Roden in carrying out the wind tunnel experiments, and of A. Klotzbach for computations. Moreover, we would like to thank H. Höche for the valuable advice on the design and cleavage of the LiF samples. Two of us (H.L. and J.P.T.) would like to thank Dr. A. K. Rebrov and his colleagues for inviting us to the Institute for Thermophysics of the Siberian Branch of the Russian Academy of Sciences in Novosibirsk in 1990, where the idea for this project was born. One of us (J.R.M.) would like to thank the Max Planck Institut für Strömungsforschung for its hospitality during the course of this work. This research was partially supported by the NSF Grant No. DMR 9726229 and by the U.S. Department of Energy under Grant No. DE-FG02-98ER45704.

APPENDIX A: FURTHER DEVELOPMENT OF THE THEORY

The differential reflection coefficient for inelastic scattering which forms the basis of the calculational model used here is developed in this Appendix. Although for the present calculations a classical inelastic scattering formalism is used, it is simplest to begin from a quantum mechanical formalism and then obtain the classical differential reflection coefficient as a limiting case of large quantum numbers of exchanged vibrational quanta. An appropriate starting point for describing a scattering process is the transition rate $w(\mathbf{p}_f, \mathbf{p}_i)$ for a particle making a transition from the initial incident beam of momentum \mathbf{p}_i to a final state denoted by momentum \mathbf{p}_f , which is given by the generalized Fermi golden rule⁷³

$$w(\mathbf{p}_f, \mathbf{p}_i) = \frac{2\pi}{\hbar} \left\langle \left\langle \sum_{\{n_f\}} |T_{fi}|^2 \delta(\mathcal{E}_f - \mathcal{E}_i) \right\rangle \right\rangle, \quad (\text{A1})$$

where the average over initial states of the crystal is denoted by $\langle\langle \rangle\rangle$, and the sum is over all final states $\{n_f\}$ of the crystal which can scatter a projectile into the specified final momentum. In Eq. (A1), the energies \mathcal{E}_i and \mathcal{E}_f refer to the total energy of the system of projectile plus the crystal before and after the collision, respectively. The T_{fi} are the matrix elements of the transition operator T taken with respect to unperturbed states of the system. All measurable quantities in a scattering experiment are proportional to the transition rate. In particular, the three-dimensional differential reflection coefficient is obtained by dividing $w(\mathbf{p}_f, \mathbf{p}_i)$ by the incident flux normal to the surface and multiplying by the appropriate density of states in final momentum space

$$\frac{dR}{d\Omega_f dE_f} = \frac{L^4}{(2\pi\hbar)^4} \frac{m^2 |\mathbf{p}_f|}{p_{iz}} w(\mathbf{p}_f, \mathbf{p}_i), \quad (\text{A2})$$

where L is the quantization length parallel to the surface.

The interaction between the atomic projectile and the surface can be described by a Hamiltonian for the entire system of the form

$$H = H^p + H^c + V, \quad (\text{A3})$$

where H^p is the Hamiltonian of the free projectile, H^c is the Hamiltonian of the unperturbed crystal, and V is the interaction coupling the projectile and crystal.

The transition operator T is related to the interaction potential through the operator equation

$$T = V + V G_0 T = V + V \frac{1}{\mathcal{E} - H^p - H^c + i\epsilon} T, \quad (\text{A4})$$

where G_0 is the Green function of the unperturbed Hamiltonian $H^p + H^c$, and the small imaginary constant $i\epsilon$ insures the proper outgoing scattering boundary conditions.

The interaction potential can be expressed as the sum of two parts

$$V = V^0 + V^1, \quad (\text{A5})$$

where the elastic part V^0 contains the major part of the potential which backscatters the projectile. V^0 is composed of a long-range attractive polarization part arising from the Van der Waals forces in front of the surface, while close to the surface V^0 becomes strongly repulsive because of the Pauli exchange exclusion forces arising from the overlap with the surface electronic density of the substrate. The remainder V^1 contains the inelastic terms describing interactions with the lattice vibrations. If the interaction potential is expanded in a Taylor series in the lattice vibrations, then

$$V = V(\mathbf{r}, \{\mathbf{u}_{j,\kappa}\})|_{\mathbf{u}_{j,\kappa}=0} + \sum_{j,\kappa} \mathbf{u}_{j,\kappa} \cdot \nabla_{j,\kappa} V(\mathbf{r}, \{\mathbf{u}_{j,\kappa}\})|_{\mathbf{u}_{j,\kappa}=0} + \dots, \quad (\text{A6})$$

where $\nabla_{j,\kappa}$ is the gradient operator with respect to the (j, κ) displacement $\mathbf{u}_{j,\kappa}$. The notation for the set of indices (j, κ) is that j is a two-dimensional variable that counts unit cells of the surface and κ is three dimensional and counts elements

of the basis set within the unit cell, including those in all the layers below the surface. Usually κ counts the crystal atoms making up the basis set of the unit cell, but this does not necessarily need to be the case. For example, for the repulsive potential due to the Pauli exclusion forces with the electron density, the potential becomes continuous in nature and it may be convenient to divide the unit cell into smaller divisions.

The logical choice is to associate V^0 with the leading term of (A6) which is now independent of the displacement, and let V^1 be the sum of all terms linear in the crystal displacement. Terms of higher order in the displacement coming from higher order in the Taylor series of Eq. (A6) contribute very little to the inelastic exchange⁷⁴ and in the classical limit can be neglected.⁴⁴

In the semiclassical limit, the transition rate of Eq. (A2) is evaluated using only classical trajectories for the scattering projectile, which leads to an expression for the differential reflection coefficient in the following form:^{25,75,76}

$$\frac{dR}{d\Omega_f dE_f} = \frac{m^2 |\mathbf{p}_f|}{8\pi^3 \hbar^5 p_{iz}} \int_{-\infty}^{+\infty} dt e^{-i\Delta E t/\hbar} \times \sum_l |\tau_{fi}^l|^2 e^{-i\mathbf{p}\cdot\mathbf{R}_l/\hbar} e^{-2W(\mathbf{p}_f, \mathbf{p}_i)} e^{2\mathcal{W}_l(\mathbf{p}_f, \mathbf{p}_i, t)}, \quad (\text{A7})$$

where the scattering momentum is $\mathbf{p} = \mathbf{p}_f - \mathbf{p}_i$, \mathbf{R}_l is the position vector of the l th unit cell of the surface, $|\tau_{fi}^l|^2$ is the form factor for scattering by the l th unit cell, $\exp\{-2W(\mathbf{p}_f, \mathbf{p}_i)\}$ is the expression for the Debye–Waller factor, $\Delta E = E_f - E_i$ is the energy gained by the projectile from the surface, and $\mathcal{W}_l(\mathbf{p}_f, \mathbf{p}_i, t)$ is a generalized correlation function. The scattering amplitude τ_{fi} comes from the potential V^0 and its square is the form factor in Eq. (A7). τ_{fi} is identified, at this level of approximation, as the transition matrix element for a unit cell of the elastic potential V^0 of Eq. (A5), extended off the energy shell. The correlation function $\mathcal{W}_l(\mathbf{p}_f, \mathbf{p}_i, t)$, which is formally a generalized time dependent pair correlation function in the crystal displacements, comes from the inelastic potential V^1 and contains the dynamics of the scattering process. In the semiclassical and classical limits it is appropriate to evaluate this correlation function in the quick collision approximation, which assumes that the collision is rapid compared to the periods of the typical phonons which are exchanged. In this case $\mathcal{W}_l(\mathbf{p}_f, \mathbf{p}_i, t)$ becomes the displacement correlation function

$$2\hbar^2 \mathcal{W}_l(\mathbf{p}, t) = \langle\langle [\mathbf{p}\cdot\mathbf{u}_0(0)\mathbf{p}\cdot\mathbf{u}_l(t)] \rangle\rangle. \quad (\text{A8})$$

The Debye–Waller factor $\exp\{-2W(\mathbf{p}_f, \mathbf{p}_i)\}$ appearing in Eq. (A7) is related to the correlation function evaluated at equal times and positions, and within the same approximations as Eq. (A8) it is the mean square displacement,

$$W(\mathbf{p}_f, \mathbf{p}_i) = \mathcal{W}_{l=0}(\mathbf{p}_f, \mathbf{p}_i, t=0) = \frac{1}{2\hbar^2} \langle\langle [\mathbf{p}\cdot\mathbf{u}_l(t)]^2 \rangle\rangle. \quad (\text{A9})$$

The displacement correlation function $\langle\langle [\mathbf{p}\cdot\mathbf{u}_0(0)\mathbf{p}\cdot\mathbf{u}_l(t)] \rangle\rangle$ is the time dependent correlation function of two

surface unit cells separated by the lattice vector \mathbf{r}_l , and can be developed in terms of the normal modes of the crystal and expressed as

$$\begin{aligned} & \langle\langle [\mathbf{p}\cdot\mathbf{u}_0(0)\mathbf{p}\cdot\mathbf{u}_l(t)] \rangle\rangle \\ &= \sum_{\alpha, \alpha'=1}^3 p_\alpha p_{\alpha'} \sum_{\mathbf{Q}, \nu} \frac{1}{2NM\hbar\omega_\nu(\mathbf{Q})} \{ [2n(\omega_\nu(\mathbf{Q})) + 1] \\ & \quad \times \cos(\omega_\nu(\mathbf{Q})t) - i \sin(\omega_\nu(\mathbf{Q})t) \}, \end{aligned} \quad (\text{A10})$$

where p_α is the α th Cartesian component of \mathbf{p} , M is the mass of a surface particle, N is the number of surface unit cells, $\omega_\nu(\mathbf{Q})$ is the normal mode frequency, and $e_\alpha(\mathbf{Q}, \nu)$ is the α th Cartesian component of the normal mode polarization vector which depends on parallel momentum \mathbf{Q} and mode index ν .

The Debye–Waller factor governs the temperature dependent attenuation of quantum mechanical features in the scattering intensity such as diffraction peaks or single phonon peaks. However, it can be shown that the argument $2W$ of the Debye–Waller function has a meaning of its own, its value is a measure of the average number of phonons transferred in a given collision. Thus values of $2W < 1$ imply purely quantum mechanical conditions in which sharp elastic peaks such as diffraction and single phonon transfers dominate the scattered intensity. Classical scattering is indicated by the condition $2W \gg 1$,²⁴ and this is the regime where the Debye–Waller factor is very small and there is negligible intensity in the quantum peaks. In the classical regime, exchange of multiple quanta dominates and there is only inelastic scattering.

A simple approximation for the Debye–Waller factor can be obtained by using a Debye model for the phonon spectrum. Then Eq. (A9) becomes, in the high temperature limit,

$$2W(\mathbf{p}) = \frac{3\mathbf{p}^2 k_B T}{M k_B^2 \Theta_D^2}, \quad (\text{A11})$$

where Θ_D is the Debye temperature.

Equation (A7), although an approximation, provides a complete quantum mechanical description of the scattering process in the sense that it includes the elastic diffraction, the single phonon (single inelastic quantum) contribution, and all higher quantum exchanges. An ordered series in numbers of exchanged phonons is obtained by expanding the term $\exp\{2\mathcal{W}_l(\mathbf{p}_f, \mathbf{p}_i)\}$ in Eq. (A7) in a series in its argument $2\mathcal{W}_l(\mathbf{p}_f, \mathbf{p}_i)$. It is of interest to note that the differential reflection coefficient for elastic scattering is identical to the exact quantum mechanical result:⁷⁵

$$\begin{aligned} \frac{dR^{(\text{el})}}{d\Omega_f dE_f} &= \sum_{\mathbf{G}} \frac{m^2 |\mathbf{p}_f|}{\hbar^4 p_{iz}} |\tau_{fi}^{\text{el}}(\mathbf{G})|^2 e^{-2W(p)} \\ & \quad \times \delta(\mathbf{P}_f - \mathbf{P}_i - \hbar\mathbf{G}) \delta(E_f - E_i), \end{aligned} \quad (\text{A12})$$

where \mathbf{G} is a reciprocal lattice vector of the surface lattice, $\tau_{fi}^{\text{el}}(\mathbf{G})$ is the elastic limit (on the energy shell) of the scattering amplitude τ_{fi} , which becomes the exact transition matrix element for the elastic potential V^0 of Eq. (A5). The

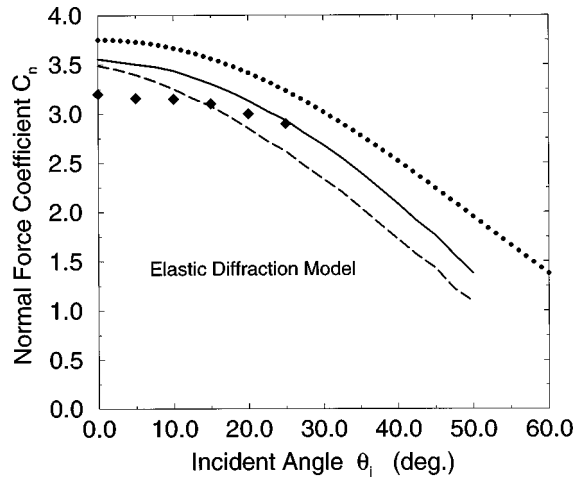


FIG. 14. Comparison of experiment (\blacklozenge) with calculations of C_n vs θ_i using the elastic diffraction differential reflection coefficient of Eq. (44) and the eikonal diffraction model of Sec. III C (elastic diffraction model). The solid curve is with the Debye–Waller factor set to unity, and the dashed curve is for $T_S=720$ K, the temperature at which the data were taken. The filled circles are the limit of free molecular flow and complete accommodation.

Dirac delta functions insure conservation of energy and allow only values of parallel momentum which satisfy the two-dimensional Bragg diffraction conditions.

The classical limit of particle scattering is characterized by high temperatures and large initial and final energies. The collision interaction is short in time and localized in space, which means that the quick collision approximation becomes exact in this limit. The surface can be treated as a two-dimensional continuum barrier. In Eq. (A7), the classical regime is characterized by the correlation function $2\mathcal{W}_l(\mathbf{p}_f, \mathbf{p}_i, t)$, becoming rapidly oscillating in both time and space. The only important contributions to the Fourier transforms of Eq. (A7) are for times $t \rightarrow 0$ and spatial positions very near to the collision point. The summations can be carried out by the method of steepest descents. The result is the differential reflection coefficient exhibited above in Eq. (19).^{25,44}

$$\frac{dR}{d\Omega_f dE_f} = \frac{m^2 v_R^2 |\mathbf{p}_f|}{4\pi^3 \hbar^2 p_{iz} S_{u.c.}} |\tau_{fi}|^2 \left(\frac{\pi}{\Delta E_0 k_B T_S} \right)^{3/2} \times \exp \left\{ - \frac{(\Delta E + \Delta E_0)^2 + 2v_R^2 P^2}{4k_B T_S \Delta E_0} \right\}. \quad (\text{A13})$$

In this classical limit, the mechanism for energy exchange is through the recoil of the surface atoms, which are initially vibrating with an equilibrium distribution of velocities. It is the initial distribution of surface atom velocities which determines the temperature dependence of the width of the scattered lobe. The dependence on incident energy and surface temperature of the full width at half maximum, in most cases, and for v_R not too large, is given to a good approximation by the following functional form:

$$\text{FWHM}^2 \propto 16 \ln(2) g E_i k_B T_S, \quad (\text{A14})$$

where g is a parameter of order unity or smaller whose angular and energy dependence is determined by the value of

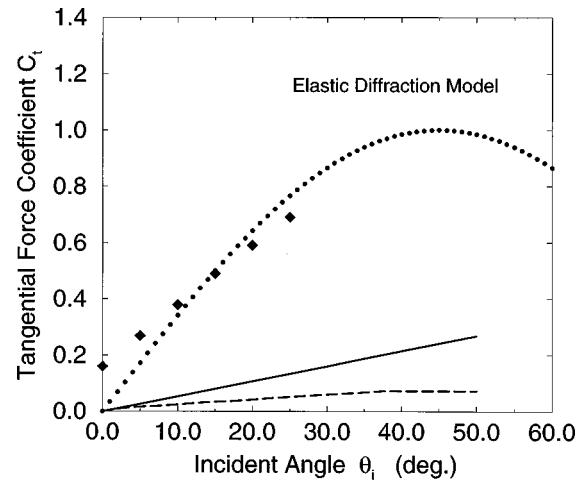


FIG. 15. Comparisons of experiment (\blacklozenge) with calculations of C_t vs θ_i using the same elastic diffraction model as in Fig. 14. The solid curve is with the Debye–Waller factor set equal to unity, and the dashed curve is with the Debye–Waller factor corresponding to the $T_S=720$ K crystal temperature at which the data were taken. The filled circle curve, for reference, is the limit of free molecular flow and complete accommodation.

v_R and by the choice of ΔE_0 and the form factor $|\tau_{fi}|^2$.^{77,78} Since the classical expression describes recoil scattering, it depends very weakly on the phonon distribution. This is evidenced by the fact that the only dependence on the details of the phonon distribution in Eq. (A13) is through the weighted average phonon speed parallel to the surface v_R . Although Eq. (A13) has a Gaussian-like form in energy and parallel momentum exchange, it is not symmetric because of the energy dependence of $\Delta E_0 = (\mathbf{p}_f - \mathbf{p}_i)^2 / 2M$. In fact, one can readily show that for $E_f \gg E_i$, Eq. (A13) is of exponential form in the energy exchange rather than Gaussian.

APPENDIX B: ELASTIC DIFFRACTION CALCULATIONS

In order to test the effects of diffraction on the force coefficients it is of interest to present some calculations based on the purely elastic differential reflection coefficient of Eq. (A12), which is called the elastic diffraction model. Although the heat transfer coefficient will vanish for elastic scattering, such is not the case for the force coefficients. Elastic scattering, while not changing the total magnitude of the momentum, does rearrange the values of the directional components of the momentum and hence can exert an impulsive force on the crystal. Such calculations are actually realistic for scattering at very low temperatures and small incident beam energies, conditions for which the exchange of energy with the surface vibrational modes becomes small.

The solid curve of Fig. 14 is an elastic diffraction calculation of the normal force coefficient C_n , using Eq. (A12) with the Debye–Waller factor set equal to unity (rigid surface limit). The scattering amplitudes are calculated in the eikonal approximation with the diffraction model of Boato *et al.* described above in Sec. III C using the usually accepted corrugation height of $A=0.145 \text{ \AA}$ [i.e., this is the elastic diffraction model of Table I with $T_S=0$ for which the Debye–Waller factor of Eq. (A12) is unity]. This calculation

is essentially a zero-temperature result, and it actually agrees with the experimental points better than the full inelastic calculation of Fig. 7. This is an interesting result because, when compared to the ordered surface calculation of Fig. 7, it implies that the effect of inelastic scattering on a perfectly ordered surface may be to enhance the average final perpendicular momentum, rather than reduce it as might be expected. For comparison, also plotted in Fig. 14 is the result of the elastic diffraction model at the experimental temperature of $T_S=720$ K, which includes the effect of the Debye-Waller factor. This $T_S \neq 0$ result gives an even smaller C_n than the $T_S=0$ case, which again supports the above statement that inclusion of vibrational degrees of freedom can enhance the final normal momentum rather than reduce it.

The results for the tangential force coefficient using the same diffraction model are shown in Fig. 15. Interestingly, this pure elastic diffraction calculation produces a significantly larger C_t at nonzero incident angles than the full inelastic calculation of Fig. 8. It would be of interest to carry out measurements at very low temperatures, both to study deviations from the results shown in Fig. 15 which would be due to surface defects, and to see if increasing the surface temperature does indeed result in smaller tangential forces on the crystal.

- ¹S. A. Schaaf and P. L. Chambré, in *High Speed Aerodynamics and Jet Propulsion*, edited by H. W. Emmons (Princeton University Press, 1958), Vol. 3, Sec. H pp. 687–739.
- ²M. Knudsen, *Ann. Phys. (Leipzig)* **32**, 809 (1910); **34**, 593 (1911).
- ³S. C. Saxena and R. K. Joshi, *Thermal Accommodation and Adsorption Coefficients of Gases, CINDAS Data Series on Material Properties*, edited by C. Y. Ho (Hemisphere, New York, 1989).
- ⁴C. Cercignani and M. Lampis, *J. Appl. Math. Phys.* **23**, 713 (1972).
- ⁵C. Cercignani and M. Lampis, *J. Appl. Math. Phys.* **27**, 733 (1976).
- ⁶C. Cercignani, *Rarefied Gas Dynamics*, edited by D. Dini, C. Cercignani, and S. Nocilla (Editrice Technico Scientifica, Pisa, 1971), Vol. 1, p. 75.
- ⁷F. O. Goodman and H. Y. Wachman, *Dynamics of Gas-Surface Scattering* (Academic, New York, 1976).
- ⁸H. Y. Wachman, *Proceedings of the 18th Rarefied Gas Dynamics Symposium* (Univ. of British Columbia, Vancouver, 1992), edited by B. Shizgal, pp. 26–31.
- ⁹H. Legge, *Heat Transfer and Forces on a LiF Single-Crystal Disc in Hypersonic Flow*, DLR-IB 222-92 A 14, DLR Göttingen (1992).
- ¹⁰We would like to thank H. Höche of the Universität Halle for help with preparing the crystals.
- ¹¹B. R. Williams, *J. Chem. Phys.* **55**, 3220 (1971).
- ¹²B. F. Mason and B. R. Williams, *J. Chem. Phys.* **57**, 872 (1972).
- ¹³B. F. Mason and B. R. Williams, *J. Chem. Phys.* **56**, 1895 (1972).
- ¹⁴J. Estel, H. Hoinkes, K. Kaarmann, H. Nahr, and H. Wilsch, *Surf. Sci.* **54**, 393 (1976).
- ¹⁵H. Kaarmann, H. Hoinkes, and H. Wilsch, *J. Chem. Phys.* **66**, 4572 (1977).
- ¹⁶H. Kaarmann, Thesis, Universität Erlangen-Nürnberg, 1975, unpublished.
- ¹⁷G. Boato, P. Cantini, and L. Mattered, *Surf. Sci.* **55**, 141 (1976).
- ¹⁸U. Garibadi, A. C. Levi, R. Spadacini, and G. E. Tommei, *Surf. Sci.* **48**, 649 (1975).
- ¹⁹G. G. Bishop, E. S. Gillman, J. Baker, J. J. Hernández, S. A. Safron, J. G. Skofronick, S. M. Weera, and J. R. Manson, *Phys. Rev. B* **52**, 13229 (1995).
- ²⁰N. Garcia and J. M. Soler, *Surf. Sci.* **126**, 689 (1983).
- ²¹D. Eichenauer and J. P. Toennies, *J. Chem. Phys.* **85**, 532 (1986).
- ²²V. Celli, D. Eichenauer, A. Kaufhold, and J. P. Toennies, *J. Chem. Phys.* **83**, 2504 (1985).
- ²³J. P. Toennies, *Proceedings of the 19th Rarefied Gas Dynamics Symposium*, Oxford University 1994.
- ²⁴H. Legge, J. P. Toennies, and J. Lüdecke, *Proceedings of the 19th Rarefied Gas Dynamics Symposium*, Oxford University 1994.
- ²⁵J. R. Manson, *Phys. Rev. B* **43**, 6924 (1991).
- ²⁶J. R. Manson, *Comput. Phys. Commun.* **80**, 145 (1994).
- ²⁷Karl Korth Kristalle GmbH, Am Jägersberg 3, 24161 Altenholz, Germany.
- ²⁸J. J. Gilman, C. Knudsen, and W. P. Walsh, *J. Appl. Phys.* **29**, 601 (1958).
- ²⁹H. Berthge, G. Kaester, and M. Krohn, *Z. Naturforsch. A* **16**, 321 (1961).
- ³⁰H. Höche and H. Berthge, *J. Cryst. Growth* **33**, 246 (1976).
- ³¹E. Meyer, H. Heinzlbaum, H. Rudin, and J. J. Günterodt, *Z. Phys. B* **79**, 3 (1990).
- ³²G. Meyer and N. M. Amer, *Appl. Phys. Lett.* **56**, 2100 (1990).
- ³³R. Lüthi, E. Meyer, M. Bammerlin, A. Baratoff, J. Lue, M. Guggidberg, C. Gerber, L. Howald, and H. J. Günterodt, *Z. Phys. B* **100**, 165 (1996).
- ³⁴R. Lüthi, M. Bammerlin, and E. Meyer, *Phys. Bl.* **53**, 435 (1997).
- ³⁵D. Schmicker, J. P. Toennies, R. Vollmer, and H. Weiss, *J. Chem. Phys.* **95**, 9412 (1991).
- ³⁶G. Lange, J. P. Toennies, R. Vollmer, and H. Weiss, *J. Chem. Phys.* **98**, 10096 (1993).
- ³⁷J. P. Toennies, in *Surface Phonons*, Springer Series in Surface Sciences **21**, edited by W. Kress and F. W. DeWette (Springer, Heidelberg, 1991), p. 111.
- ³⁸G. Lillienkamp and J. P. Toennies, *J. Chem. Phys.* **78**, 5210 (1983).
- ³⁹G. Brusdeylins, R. B. Doak, and J. P. Toennies, *Phys. Rev. Lett.* **44**, 1417 (1980).
- ⁴⁰G. Brusdeylins, R. B. Doak, and J. P. Toennies, *Phys. Rev. Lett.* **46**, 437 (1981).
- ⁴¹G. Brusdeylins, R. B. Doak, and J. P. Toennies, *Phys. Rev. B* **27**, 3662 (1983).
- ⁴²S. R. Cook, J. B. Cross, and M. Hoffbauer, *Proceedings of the 18th Aerospace Ground Testing Conference*, Colorado Springs, CO, 1994.
- ⁴³G. E. Caledonia, R. H. Krech, B. L. Upschulte, K. W. Holtzclaw, and D. B. Oakes, *Proceedings of the 18th Aerospace Ground Testing Conference*, Colorado Springs, CO, 1994.
- ⁴⁴R. Brako and D. M. Newns, *Phys. Rev. Lett.* **48**, 1859 (1982); *Surf. Sci.* **123**, 439 (1982).
- ⁴⁵K. Burke, B. Gumhalter, and D. C. Langreth, *Phys. Rev. B* **47**, 12852 (1993).
- ⁴⁶V. Celli, G. Benedek, U. Harten, J. P. Toennies, R. B. Doak, and V. Bortolani, *Surf. Sci.* **143**, 376 (1984).
- ⁴⁷F. Hofmann, J. P. Toennies, and J. R. Manson, *J. Chem. Phys.* **101**, 10155 (1994).
- ⁴⁸G. G. Bishop, W. P. Brug, G. Chern, J. Duan, S. A. Safron, J. G. Skofronick, and J. R. Manson, *Phys. Rev. B* **47**, 3966 (1993).
- ⁴⁹R. B. Doak, Thesis, Göttingen University, 1982, unpublished.
- ⁵⁰G. W. Farnell, in *Physical Acoustics*, edited by W. P. Mason and R. N. Thurston (Academic, New York, 1970), Vol. 6, pp. 109–166.
- ⁵¹S. M. Weera, J. R. Manson, E. S. Gillman, J. Baker, J. J. Hernández, G. G. Bishop, S. A. Safron, and J. G. Skofronick, *Phys. Rev. B* **52**, 14185 (1995).
- ⁵²F. Hofmann, J. R. Manson, and J. P. Toennies, *Surf. Sci.* **349**, 184 (1996).
- ⁵³B. Gumhalter and A. Bilić, *Surf. Sci.* **370**, 47 (1996).
- ⁵⁴G. Armand and J. R. Manson, *Phys. Rev. B* **25**, 6195 (1982).
- ⁵⁵J. Lapujoulade, J. Perreau, and A. Kara, *Surf. Sci.* **129**, 59 (1983); G. Armand, J. Lapujoulade, and Y. Lejay, *Proc. 7th International Vacuum Congress and 3rd International Conference on Solid Surfaces*, Vienna, 1977, edited by R. Dobrozemsky *et al.*, p. 1361.
- ⁵⁶M. Foss, F. Besenbacher, C. Klink, and I. Stensgard (unpublished).
- ⁵⁷N. Bunjes, N. S. Luo, P. Ruggerone, J. P. Toennies, and G. Witte, *Phys. Rev. B* **50**, 8897 (1994).
- ⁵⁸J. M. Home, C. Yerkes, and D. R. Miller, *Surf. Sci.* **93**, 47 (1980).
- ⁵⁹G. Rovida, M. Torrini, and E. Zanizzi, *Nuovo Cimento B* **4**, 97 (1971).
- ⁶⁰V. Bortolani, A. Franchini, N. Garcia, F. Nizzoli, and G. Santoro, *Phys. Rev. B* **28**, 7358 (1983).
- ⁶¹J. P. Toennies, G. Witte, and Ch. Wöll (unpublished).
- ⁶²D. G. Castner, G. A. Somorjai, J. E. Black, D. Castiel, and R. F. Wallis, *Phys. Rev. B* **24**, 1616 (1981).
- ⁶³K. Kern, Ph.D. thesis, University of Bonn, Jülich, 1985, unpublished.
- ⁶⁴H. B. Lyon and G. A. Somorjai, *J. Chem. Phys.* **44**, 3707 (1966).
- ⁶⁵D. R. Hamann, *Phys. Rev. Lett.* **46**, 1227 (1981).
- ⁶⁶A. Lock, *Diplom Thesis at University Göttingen*, 1987.
- ⁶⁷A. Muis and J. R. Manson, *Phys. Rev. B* **54**, 2205 (1996).
- ⁶⁸G. Benedek, J. Ellis, N. S. Luo, A. Reichmuth, P. Ruggerone, and J. P. Toennies, *Phys. Rev. B* **48**, 4917 (1993).
- ⁶⁹N. W. Ashcroft and N. D. Mermin, *Solid State Physics* (Saunders, Philadelphia, 1976), p. 456.

- ⁷⁰G. Armand and J. R. Manson, Phys. Rev. B **43**, 14371 (1991).
- ⁷¹S. Andersson, L. Wilzén, M. Persson, and J. Harris, Phys. Rev. B **40**, 8146 (1989).
- ⁷²M. Persson, Phys. Rev. B **36**, 7870 (1987).
- ⁷³L. S. Rodberg and R. M. Thaler, *Quantum Theory of Scattering* (Academic, New York, 1967).
- ⁷⁴G. Armand and J. R. Manson, Phys. Rev. Lett. **53**, 1112 (1985); C. S. Jayanthi, G. Armand, and J. R. Manson, Surf. Sci. **154**, 247 (1985); G. Armand and J. R. Manson, J. Phys. (Paris) **47**, 1357 (1986).
- ⁷⁵V. Bortolani and A. C. Levi, Riv. Nuovo Cimento **9**, 1 (1986).
- ⁷⁶A. Sjölander, Ark. Fys. **14**, 315 (1959).
- ⁷⁷C. A. DiRubio, D. M. Goodstein, B. H. Cooper, and K. Burke, Phys. Rev. Lett. **73**, 2768 (1994).
- ⁷⁸A. Muis and J. R. Manson, J. Chem. Phys. **107**, 1655 (1997).